

Scaling the ion inertial length and its implications for modeling reconnection in global simulations

Gábor Tóth¹, Yuxi Chen¹, Tamas I. Gombosi¹, Paul Cassak², Stefano Markidis³, Ivy Bo Peng³

¹ Center for Space Environment Modeling, University of Michigan, Ann Arbor, MI, USA.

² Department of Physics and Astronomy, West Virginia University, Morgantown, WV, USA.

³ KTH, Stockholm, Sweden.

Key Points:

- Magnetohydrodynamics with Embedded Particle-in-Cell magnetospheric simulations with increased kinetic scales.
- Changing the kinetic scales does not change the global solution significantly.
- Increasing the kinetic scales makes global simulations with embedded kinetic regions feasible.

This is the author manuscript accepted for publication and has undergone full peer review but has not been through the copyediting, typesetting, pagination and proofreading process, which may lead to differences between this version and the [Version of Record](#). Please cite this article as doi: [10.1002/2017JA024189](https://doi.org/10.1002/2017JA024189)

Abstract

We investigate the use of artificially increased ion and electron kinetic scales in global plasma simulations. We argue that as long as the global and ion inertial scales remain well separated, 1) the overall global solution is not strongly sensitive to the value of the ion inertial scale, while 2) the ion inertial scale dynamics will also be similar to the original system, but it occurs at a larger spatial scale, and 3) structures at intermediate scales, such as magnetic islands, grow in a self-similar manner. To investigate the validity and limitations of our scaling hypotheses, we carry out many simulations of a two-dimensional magnetosphere with the magnetohydrodynamics with embedded particle-in-cell (MHD-EPIC) model. The PIC model covers the dayside reconnection site. The simulation results confirm that the hypotheses are true as long as the increased ion inertial length remains less than about 5% of the magnetopause standoff distance. Since the theoretical arguments are general, we expect these results to carry over to three dimensions. The computational cost is reduced by the third and fourth powers of the scaling factor in two- and three-dimensional simulations, respectively, which can be many orders of magnitude. The present results suggest that global simulations that resolve kinetic scales for reconnection are feasible. This is a crucial step for applications to the magnetospheres of Earth, Saturn and Jupiter and to the solar corona.

1 Introduction

Plasma systems are often characterized by large separation of spatial and temporal scales. In the magnetospheres of Earth, Saturn and Jupiter, or in the solar corona, the ion kinetic scales characterized by the ion inertial length d_i are orders of magnitude smaller than the global scales of the system d_g characterized by the magnetopause standoff distance or some fraction of the solar radius. Electron scales characterized by the electron skin depth d_e are even smaller. Systems with a broad range of temporal and spatial dynamical scales present observational, theoretical as well as computational challenges.

In some special cases, for example shock waves in an ideal neutral gas, the global behavior does not depend on the details of the small scale physics, because the jump conditions across a hydrodynamic shock are fully determined by the conservation of mass, momentum and energy. For more complicated systems, such as magnetohydrodynamics with anisotropic ion pressure, the conservation laws constrain the jump conditions, but the

45 pressure anisotropy behind the shock cannot be determined without knowledge of small
46 scale processes.

47 Magnetic reconnection is even more complex and challenging. In general, the global
48 dynamics roughly determines the possible locations where reconnection can occur, but
49 reconnection is a dynamic process with complex behavior. Even for the simplest magne-
50 tohydrodynamic description of plasma, the energy conservation law only tells us that the
51 magnetic energy will be converted into other forms of energy, but it does not predict in
52 general how fast the energy conversion will occur, or how the converted energy will be
53 distributed between bulk kinetic and thermal energies. If we allow for pressure anisotropy
54 and separate electron and ion temperatures, the outcome of the reconnection process is
55 even less determined by simple conservation laws, and more dependent on the small scale
56 processes.

57 While magnetic reconnection occurs on the kinetic scales, it is well known that re-
58 connection can globally affect systems of much larger size. Some typical examples are the
59 magnetospheres of planets or the solar corona, where reconnection plays a crucial role in
60 global phenomena, such as magnetic storms and coronal mass ejections. If we are inter-
61 ested in the interplay between the global plasma system and the reconnection process, it
62 is a natural question to ask how the behavior of the system depends on the ratio d_g/d_i .
63 Clearly, if d_g/d_i is a relatively small number (order of 10 or less), the kinetic effects will
64 have a direct impact on the global solution, even if no reconnection occurs. For example,
65 in Ganymede's magnetosphere $d_g/d_i \approx 10$ and indeed the ideal or resistive MHD [Dorelli *et al.*, 2015]
66 that neglect the Hall effect are globally different from the Hall MHD [Dorelli *et al.*, 2015]
67 or the magnetohydrodynamics with embedded particle-in-cell (MHD-EPIC) solution [Tóth
68 *et al.*, 2016]. On the other hand, if d_g/d_i is a very large number, then the kinetic effects
69 will be mostly limited to the reconnection region. There can be other kinetic effects that
70 may act on a larger scale (for example, foreshock waves, energetic particles, etc.) but in
71 this work we concentrate on systems, where the kinetic effects of interest are limited to
72 the reconnection process.

73 The main question we are going to address in this work is how the coupled global-
74 kinetic system depends on the value of d_g/d_i when it is large versus extremely large, and
75 how we can change this scale separation. Let us examine the various kinetic length scales
76 and see if there is a way to change them. The smallest plasma scale, where significant

charge separation may occur, is given by the Debye length (in SI units) as

$$\lambda_D = \sqrt{\frac{\epsilon_0 v_{th,e}^2}{q_e^2 n_e}} = \frac{m_e}{q_e} \frac{\sqrt{\epsilon_0 p_e}}{\rho_e} \quad (1)$$

where m_e is the electron mass, $q_e > 0$ is the elementary charge, n_e and ρ_e are the electron number and mass densities, respectively, ϵ_0 is the permittivity of vacuum, $v_{th,e} = \sqrt{p_e/\rho_e}$ is the electron thermal velocity and p_e is the electron pressure.

The change of magnetic topology during collisionless magnetic reconnection occurs in the electron diffusion region [Vasyliunas, 1975]. For antiparallel reconnection the characteristic size is the electron skin depth

$$d_e = \sqrt{\frac{m_e}{n_e q_e^2 \mu_0}} = \frac{m_e}{q_e} \sqrt{\frac{1}{\rho_e \mu_0}} \quad (2)$$

where $\mu_0 = 1/(c^2 \epsilon_0)$ is the magnetic permeability of vacuum and c is the speed of light, so $\lambda_D = (v_{th,e}/c)d_e$. If the electron thermal velocity is much less than the speed of light, the Debye length is much smaller than the electron skin depth. A standard trick to reduce this separation of scales is to artificially reduce the speed of light to a value that is still larger than the thermal and bulk velocities, but not many orders of magnitude larger.

When there is a significant guide field, the electron scales are determined by the electron gyro radius

$$r_e = \frac{v_{th,e} m_e}{q_e B} = \frac{m_e}{q_e} \frac{\sqrt{p_e/\rho_e}}{B} \quad (3)$$

where B is the magnetic field strength. When the electron thermal velocity $v_{th,e}$ equals the electron Alfvén speed $v_{A,e} = B/\sqrt{\mu_0 \rho_e}$, then the electron gyro radius r_e equals the electron skin depth d_e , so in the vicinity of reconnection sites r_e and d_e are typically comparable.

The characteristic scales for kinetic ion physics are given by the ion inertial length

$$d_i = \sqrt{\frac{m_i}{n_i q_i^2 \mu_0}} = \frac{m_i}{q_i} \sqrt{\frac{1}{\rho_i \mu_0}} \quad (4)$$

and the ion gyro radius

$$r_i = \frac{v_{th,i} m_i}{q_i B} = \frac{m_i}{q_i} \frac{\sqrt{p_i/\rho_i}}{B} \quad (5)$$

These are $\sqrt{m_i/m_e}$ times larger than the corresponding electron length scales d_e and r_e , respectively, assuming that $n_i = n_e$ (which implies $\rho_i/\rho_e = m_i/m_e$), $q_i = q_e$ and $p_i = p_e$. For a proton-electron plasma $d_i/d_e = \sqrt{1836} \approx 43$. This ratio already presents a daunting challenge to computational models, especially in three dimensions (3D), since one

101 needs to model hundreds of d_i in each spatial dimension. A standard trick is to arti-
102 cially reduce the mass ratio to a smaller value, anywhere from 25 and higher. Such a tech-
103 nique is only allowable if using an unrealistic ion to electron mass ratio does not greatly
104 change the reconnection process. There have been numerous studies [*Shay and Drake,*
105 *1998; Hesse et al., 1999; Ricci et al., 2004; Shay et al., 2007; Lapenta et al., 2010*] that
106 found only a relatively weak dependence of the reconnection process on the mass ratio.
107 In practice almost all numerical studies, especially in 3D, use a reduced ion-electron mass
108 ratio.

109 Here we propose to use a similar trick to change the ion and electron scales relative
110 to the global scale d_g . The kinetic length scales defined in equations 1–5 are all propor-
111 tional to the mass to charge ratios m_e/q_e and m_i/q_i . *We will therefore increase the ion and*
112 *electron mass to charge ratios by a kinetic scaling factor f* while keeping the MHD quan-
113 tities, the mass densities ρ_e and ρ_i , the pressures p_e and p_i , the bulk velocities \mathbf{u}_e and
114 \mathbf{u}_i , the magnetic field \mathbf{B} , and the various constants ϵ_0 , μ_0 and c unchanged. Note that the
115 characteristic speeds (bulk velocity, thermal velocity, Alfvén speed) are not affected by the
116 scaling. In fact, the proposed *kinetic scaling* has no effect on ideal or resistive MHD.

117 As long as the scaled d_g/d_i ratio remains large enough, it is plausible that the global
118 solution might not be sensitive to the actual value of d_i due to the separation of scales.

119 We hypothesize that

- 120 1. The solution on the global scales does not depend sensitively on f .
- 121 2. The solution on the kinetic scales is similar for different values of f but the spatial
122 and temporal scales are proportional to f .
- 123 3. Structures forming at the kinetic scales and growing to the global scales follow a
124 self-similar growth at the intermediate scales.

125 In this paper we will conduct numerical experiments to see whether these statements hold
126 true or not and what their limitations are. These numerical experiments require that the
127 model captures both the global and the kinetic scales. With a pure kinetic code the sim-
128 ulations would be computationally extremely expensive, even in two spatial dimensions
129 (2D). Fortunately, the simulations can be performed with the MHD-EPIC method [*Dal-*
130 *dorff et al., 2014; Tóth et al., 2016*]: the MHD model provides the global solution while
131 the embedded PIC model simulates the reconnection region. The MHD model BATS-

132 R-US [Powell *et al.*, 1999; Tóth *et al.*, 2012] employs a block-adaptive mesh refinement
133 (AMR) for sake of efficiency, while the PIC model is the implicit particle-in-cell code
134 iPIC3D [Markidis *et al.*, 2010] that uses a semi-implicit scheme [Brackbill and Forslund,
135 1982] to allow larger grid cell sizes and time steps than the explicit PIC algorithms. The
136 MHD and PIC models are efficiently coupled through the Space Weather Modeling Frame-
137 work (SWMF) [Tóth *et al.*, 2005, 2012, 2016].

138 Independent of the numerical method employed, the ratio of the global and kinetic
139 scales has a tremendous impact on the computational cost of global simulations that ac-
140 count for kinetic effects. The required grid cell size is proportional to f , so the number of
141 grid cells and macro-particles is proportional to f^{-D} , where D is the number of spatial di-
142 mensions. In addition, the time step limited by stability and/or accuracy constraints is also
143 proportional to f , so the computational cost of advancing the simulation to a given sim-
144 ulation time is reduced by a factor of f^3 in 2D and factor of f^4 in 3D. In addition to the
145 theoretical interest in the scaling properties of the reconnection process, these computational
146 benefits are a major motivation of our work. Using the kinetic scaling makes it possible
147 to perform 3D global simulations of Earth's magnetosphere while using a kinetic model to
148 capture the reconnection process, as demonstrated in our companion paper by *Chen et al.*
149 [2017, accepted companion paper].

150 In the following sections we will briefly describe the theoretical arguments behind
151 our scaling hypothesis, the numerical models, the simulation set up and then discuss the
152 results of the numerical experiments.

153 **2 Theoretical arguments**

154 Here we present some theoretical arguments in support of our hypothesis. This is
155 not intended to be a proof, rather, we argue that the scaling is plausible.

156 **2.1 Global scales: insensitivity**

157 The main role of magnetic reconnection in the global dynamics of Earth's magneto-
158 sphere is to drive magnetospheric convection. The aspect of reconnection that determines
159 the global response is the reconnection rate. In particular, if reconnection is slow or non-
160 existent, such as for due northward interplanetary magnetic field (IMF) in the absence of
161 a dipole tilt, the magnetospheric response is minimal. If reconnection is present and effi-

162 cient (such as when the interplanetary magnetic field has a southward component), then
163 the Dungey cycle of magnetospheric convection occurs. Thus, the bare minimum require-
164 ment to capture the global scale response is an accurate representation of the reconnection
165 rate. Similar arguments apply to other global systems that involve reconnecting magnetic
166 fields.

167 A significant amount of research has gone into determining the reconnection rate
168 for collisionless plasmas. It has been established by several kinetic modeling studies of
169 symmetric anti-parallel reconnection in a rectangular two-dimensional domain [*Shay et al.*,
170 1999; *Birn et al.*, 2001; *Huba and Rudakov*, 2004; *Schoeffler et al.*, 2012] that the steady-
171 state reconnection rate, quantified as the reconnection electric field E , is about 0.1 times
172 the reconnecting magnetic field strength B_r times the Alfvén speed $v_{Ar} = B_r / \sqrt{\mu_0 \rho}$ out-
173 side the current sheet. Insight on why the normalized reconnection rate $E / (B_r v_{Ar}) \approx 0.1$
174 seems to be independent of system parameters has only been achieved recently [*Liu et al.*,
175 2017].

176 At the dayside magnetopause, the reconnection is asymmetric with different mag-
177 netic field strengths, densities, and temperatures on the two sides of the reconnection re-
178 gion. It was shown that the asymmetric reconnection rate, in 2D anti-parallel reconnection
179 in a rectangular domain, is also 0.1 when normalized to a suitably defined hybrid Alfvén
180 speed and magnetic field [*Cassak and Shay*, 2007]. There is also observational support for
181 this prediction [*Mozzer and Hull*, 2010].

182 Thus, both for symmetric and asymmetric reconnection, the reconnection rate is ex-
183 pected to be of the form $E \sim 0.1 v_{Ar} B_r$. This is important for the present study, because
184 both B_r and the Alfvén speed v_{Ar} are purely MHD-scale quantities that are not affected
185 by the kinetic scale governed by f . In other words, the reconnection rate is not sensitive
186 to f , and therefore the overall global-scale solution will be insensitive to f .

187 The other important product of reconnection that can affect global dynamics is the
188 production of magnetic islands. This process starts with the tearing instability. The growth
189 rate of the individual islands depends on the reconnection rate. In addition, the islands
190 may coalesce and merge. The interaction of magnetic islands is a complex and somewhat
191 chaotic process for an infinite (e.g. Harris type) current sheet, because in that system there
192 is no global scale along the current sheet (other than the size of the simulation box) that
193 would organize the dynamics. The situation is different when the current sheet has a finite

194 length because it is part of a global system and there is significant plasma flow along the
195 current sheet.

196 In the dayside magnetosphere, for example, the curvature of the magnetopause and
197 the magnetosheath flows have a strong influence on the motion of the magnetic islands,
198 or in magnetospheric terms, the flux transfer events (FTEs). The FTEs are swept either
199 northward or southward by the bulk flow, and their growth stops when they reach the end
200 of the current sheet at the cusps. Similarly, in the magnetotail, the overall plasma convec-
201 tion will push the magnetic islands, often called plasmoids, either tailward or planetward,
202 and their time to grow is limited by the extent of the tail current sheet.

203 The reconnection rate governing the growth rate, and the plasma flow speed and the
204 extent of the current sheet determining the life time of the magnetic islands are indepen-
205 dent of the kinetic scaling factor f , therefore we expect the global dynamics to be insensi-
206 tive to the value of f .

207 **2.2 Kinetic scales: proportionality**

208 If we place ions and electrons into a box, the spatial scale of the various structures
209 formed by them will depend on the electron and ion scales (λ_D , d_e , r_e , d_i and r_i) and the
210 initial and boundary conditions.

211 Kinetic simulations often employ periodic boundary conditions. If the computational
212 domain is large enough and the initial conditions don't have any scales, for example the
213 plasma has uniform density, pressure and velocity and the magnetic field is also constant,
214 then the solution will scale purely with the electron and ion length scales that are all pro-
215 portional to the mass per charge ratios m_e/q_e and m_i/q_i . The same holds if the initial
216 conditions are not uniform, but contain a discontinuity, such as a sharp current sheet, be-
217 cause a discontinuity does not introduce any length scale. In fact, most kinetic simulation
218 results are presented in length units normalized to d_i and time normalized to the inverse
219 of the ion cyclotron frequency. Of course, one may introduce a global scale into the sys-
220 tem through the initial conditions, but here we are interested in structures formed sponta-
221 neously by the reconnection process, and the size of those structures will scale with the
222 kinetic length scales.

223 When the box is part of a global system, the boundary conditions applied to the
224 box will have an influence. We assume that the boundary conditions are well described
225 by MHD quantities, so the deviations from a Maxwellian distribution are relatively small
226 at the boundaries. In the simplest case the boundary conditions are homogeneous (con-
227 stant density, velocity, pressure and magnetic field), so no global scales are introduced into
228 the system. A slightly more complicated example is when there is a discontinuity in the
229 boundary conditions, for example a current sheet. Again, no global length scale is intro-
230 duced. In the most general case, of course, the boundary and initial conditions will have
231 gradients and higher derivatives that introduce a global scale d_g . Our hypothesis states
232 that as long as $\varepsilon = d_i/d_g$ is much smaller than 1, the spatial scales of the reconnection
233 dynamics will be predominantly determined by d_i and d_e and will not be sensitive to d_g .

234 **2.3 Intermediate scales: self-similarity**

235 We argued in the previous two sub-sections that the global dynamics are determined
236 by MHD quantities, while the kinetic scales are proportional to f . What about structures
237 that start at the kinetic scales and grow to the global scales? For example, magnetic is-
238 lands (flux transfer events, plasmoids) are initiated at the kinetic scale that is proportional
239 to f , and they grow in size to the global scales. Depending on f , the FTEs will be at
240 different stages of their evolution (characterized by their size s relative to d_i) when they
241 reach the global scale ($s \propto d_g$). The only way these structures will look similar at the
242 global scale is if their evolution is self-similar at the intermediate scales.

243 Self-similar solutions arise naturally for PDEs that have no inherent length and time
244 scales. If the initial conditions do not define a length scale, for example it consists of two
245 uniform states separated by a discontinuity (shock-tube problems), the solution will be
246 self-similar. The Euler equations and the ideal MHD equations are two examples for PDEs
247 without any inherent length or time scales. The Navier-Stokes equations have an inher-
248 ent length scale due to viscosity, and similarly the Hall MHD equations have an inherent
249 length scale of the ion inertial length. As long as these are very small, we may expect that
250 the evolution will become self-similar once the size s is much larger than the kinetic scale
251 d_i but still small relative to the global scales d_g . For the Vlasov equations there are two
252 inherent length scales, the ion scales characterized by d_i and the electron scales given by
253 d_e , but the above argument still applies as long as the ratio $d_i/d_e = \sqrt{m_i/m_e}$ is kept con-
254 stant while changing f , or if they are also well separated: $d_i \gg d_e$.

255 In the collisionless reconnection process multiple magnetic islands of different sizes
256 form near each other, they interact with each other and often merge to form larger islands.
257 This is a much more complicated process than the growth of an individual island. Still, it
258 is plausible to assume that the end result of these interactions at a fixed intermediate scale
259 will look similar independent of the scaling of the much smaller kinetic scales. Similar
260 ideas of self-similar plasmoid driven reconnection have been suggested and numerically
261 studied by *Shibata and Tanuma* [2001], *Nitta et al.* [2002], *Schoeffler et al.* [2012], and
262 *Tenerani et al.* [2015].

263 **3 MHD-EPIC model**

264 The magnetohydrodynamics with embedded PIC algorithm (MHD-EPIC) [*Daldorff*
265 *et al.*, 2014] couples an MHD and a PIC model both ways. First the MHD model pro-
266 duces a solution in the full computational domain that covers the global system. Next, one
267 or more PIC regions are selected based on the sites of interest, such as reconnection sites.
268 The PIC model is initialized with the MHD solution in the PIC regions by generating
269 macro-particles with the proper mass density, velocity and pressure assuming Maxwellian
270 distribution functions. From this point on, the PIC model solves the Vlasov-Maxwell
271 equations as usual, and the MHD solution is completely overwritten inside the PIC re-
272 gions based on the moments of the distribution functions obtained by the PIC model. The
273 boundary conditions of the PIC model are provided by the MHD model at the boundaries
274 of the PIC regions that are placed far enough from the reconnection sites so that the MHD
275 approximation is valid. The MHD and PIC models exchange information periodically until
276 the simulation is stopped. The coupling is performed in an efficient manner using parallel
277 message passing through the SWMF. The BATS-R-US grid blocks that interact with the
278 PIC region(s) are distributed evenly among the processors to improve the load balance.
279 Typically the coupling uses only a few percent of the total computational time.

280 The original MHD-EPIC algorithm [*Daldorff et al.*, 2014] has been extended in sev-
281 eral ways:

- 282 1. The MHD and PIC grids do not need to be aligned or have the same resolution.
- 283 2. The MHD grid can be non-Cartesian.
- 284 3. The MHD and PIC models may take different time steps.
- 285 4. Multi-species and multi-ion (Hall) MHD can be coupled with the PIC model.

286 The first two improvements allow more flexibility in the choice of the spatial discretization
 287 for the MHD model and also in the placement of the PIC region in the global domain.
 288 The third improvement makes the model more robust as it allows both models to adjust
 289 their time steps based on their respective stability and/or accuracy conditions. In fact, the
 290 iPIC3D code now has the option to adjust its time step based on the electron particle ve-
 291 locities and the cell size as $\Delta t_{\text{PIC}} = C \min(\Delta s_{\text{PIC}}/v_{e,rms})$ where Δs_{PIC} is the smallest di-
 292 mension of the PIC grid cells and $v_{e,rms}$ is the root mean square of the macro-particle
 293 electron velocities calculated in each PIC grid cell. The minimum is taken over all the
 294 PIC grid cells. The C coefficient should be less than one to maintain accuracy. We set
 295 $C = 0.4$ in all simulations. The BATS-R-US code also sets the time step based on the sta-
 296 bility conditions. The coupling frequency is usually set to be close to the typical value of
 297 the larger of the MHD and PIC time steps.

298 The last improvement means that the MHD-EPIC model now allows the MHD code
 299 to solve the multi-species, multi-ion and two-fluid MHD equations. In this work BATS-R-
 300 US solves the two-fluid equations, i.e. the Hall MHD equations together with a separate
 301 electron pressure equation:

$$\frac{\partial \rho}{\partial t} + \nabla \cdot (\rho \mathbf{u}) = 0 \quad (6)$$

$$\frac{\partial \rho \mathbf{u}}{\partial t} + \nabla \cdot \left[\rho \mathbf{u} \mathbf{u} + I \left(p + p_e + \frac{B^2}{2\mu_0} \right) - \frac{\mathbf{B}\mathbf{B}}{\mu_0} \right] = 0 \quad (7)$$

$$\frac{\partial \mathbf{B}}{\partial t} + \nabla \times \mathbf{E} = 0 \quad (8)$$

$$\frac{\partial e}{\partial t} + \nabla \cdot \left[\mathbf{u} \left(\frac{1}{2} \rho u^2 + \frac{\gamma p}{\gamma - 1} \right) + \mathbf{u}_e p_e + \frac{\mathbf{E} \times \mathbf{B}}{\mu_0} \right] = p_e \nabla \cdot \mathbf{u}_e \quad (9)$$

$$\frac{\partial p_e}{\partial t} + \nabla \cdot (p_e \mathbf{u}_e) = -(\gamma - 1) p_e \nabla \cdot \mathbf{u}_e \quad (10)$$

302 where I is the identity matrix, $\gamma = 5/3$ is the adiabatic index both for ions and electrons,
 303 ρ , \mathbf{u} and p are the mass density, bulk velocity and pressure of ions,

$$\mathbf{u}_e = \mathbf{u} - \frac{\mathbf{J}}{q_e n_e} = \mathbf{u} - \frac{m_i}{q_i} \frac{\mathbf{J}}{\rho} \quad (11)$$

304 is the electron velocity, $\mathbf{J} = \nabla \times \mathbf{B} / \mu_0$ is the current density,

$$\mathbf{E} = -\mathbf{u}_e \times \mathbf{B} - \frac{\nabla p_e}{n_e q_e} + \eta \mathbf{J} = -\mathbf{u} \times \mathbf{B} + \frac{m_i}{q_i} \frac{\mathbf{J} \times \mathbf{B} - \nabla p_e}{\rho} + \eta \mathbf{J} \quad (12)$$

305 is the electric field, η is the resistivity, and

$$e = \frac{p}{\gamma - 1} + \frac{\rho u^2}{2} + \frac{B^2}{2\mu_0} \quad (13)$$

306 is the total ion plus magnetic energy density. Note that the electron thermal energy is not
 307 included, which explains the source term on the right hand side of equation 9. This choice

308 does not affect the energy conservation properties, since the sum of the energy equation 9
309 and $1/(\gamma - 1)$ times the electron pressure equation 10 gives the total energy conserva-
310 tion law with no source terms both analytically and in the discretized form. Note that the
311 electron-ion energy exchange term is ignored for this collisionless plasma. In fact, colli-
312 sional resistivity is also zero in reality, and we only use it for setting up the initial condi-
313 tions as discussed in the next section.

314 **4 Numerical Schemes**

315 In the simulations presented here, BATS-R-US uses the second order total variation
316 diminishing scheme [van Leer, 1979] with Rusanov flux function [Rusanov, 1961] and Ko-
317 ren's limiter [Koren, 1993] with the parameter $\beta = 1.2$. The initial conditions are obtained
318 with BATS-R-US only by solving the resistive MHD equations with a constant magnetic
319 diffusivity $\eta/\mu_0 = 10^{10} \text{ m}^2/\text{s}$ applied in the induction equation. The only goal of using re-
320 sistivity is to make the current sheets smooth and stable (no islands); therefore the Joule
321 heating and the heat exchange terms between the electrons and ions are switched off to
322 avoid unwanted heating of the electrons and thermal equilibration between the ions and
323 electrons. We run BATS-R-US in local time stepping mode [Tóth *et al.*, 2012] for 10,000
324 iterations to reach the steady state.

325 The time dependent simulations start from this initial steady state solution. BATS-
326 R-US solves the two-fluid MHD equations with the Hall and electron pressure gradient
327 terms in the induction equation, but no resistivity. To avoid the time step limitation due
328 to the whistler waves, a semi-implicit time discretization is used for the Hall term. The
329 numerical diffusion due to the whistler speed is reduced by a factor of ten similar to the
330 reduction used in the fully implicit Hall MHD scheme [Tóth *et al.*, 2008].

331 We use the 8-wave scheme [Powell, 1994] in combination with hyperbolic/parabolic
332 cleaning [Dedner *et al.*, 2003] to control the numerical divergence of the magnetic field.
333 Usually the 8-wave scheme is sufficient in pure MHD and Hall-MHD simulations, but
334 for MHD-EPIC there is a problem: the divergence error (that is advected by the 8-wave
335 scheme together with the plasma) cannot propagate through the PIC region, since iPIC3D
336 does not use the 8-wave scheme. As a result, the divergence errors can accumulate at the
337 boundary of the PIC region. Using the hyperbolic/parabolic cleaning helps, because it can
338 dissipate the divergence error in all directions, not only along stream lines. We set the hy-

339 perbolic speed parameter to $c_h = 400 \text{ km/s}$ and the parabolic decay parameter to $c_p = 0.1$
 340 (see *Dedner et al.* [2003] and *Tóth et al.* [2012]).

341 The iPIC3D code solves the Maxwell equations for the electric and magnetic fields
 342 and the equations of motion for the particles as usual [*Markidis et al.*, 2010]. It uses an
 343 implicit scheme [*Brackbill and Forslund*, 1982] to solve for the electric field to avoid the
 344 numerical stability issues that restrict the cell size Δx to be less than the Debye length λ_D
 345 and the time step Δt to be smaller than $\Delta x/c$ (the time it takes for light wave to cross a
 346 grid cell) in explicit PIC codes. Even for a semi-implicit PIC code, using the true speed
 347 of light, while possible, is computationally expensive, because it makes the linear problem
 348 to be solved stiffer, requiring more iterations. It is therefore standard practice to ar-
 349 tificially lower the speed of light c to a reduced value c' that is still large relative to the
 350 flow speeds. This trick, also used in MHD codes (named the semi-relativistic or Boris
 351 correction [*Boris*, 1970; *Gombosi et al.*, 2002]) exploits the separation of scales between
 352 the speed of light and the speed of the plasma flow speeds. In these simulation we used
 353 $c' = 3000 \text{ km/s}$. To reduce the scale separation of the electron skin depth and ion inertial
 354 length, the ion-electron mass ratio is set to $m_i/m_e = 100$. In all simulations each PIC grid
 355 cell is initialized with 225 ion and 225 electron macro-particles, and the same number of
 356 particles are generated in the PIC grid ghost cells during the MHD-EPIC coupling.

357 We also find it useful to suppress some short wavelength oscillations that are gen-
 358 erated in the PIC region. These oscillations appear to be related to Langmuir waves, and
 359 they reach significant amplitudes in 2D simulations (the issue seems to be less significant
 360 in 3D simulations). A relatively simple way to suppress these waves is the smoothing of
 361 the electric field at short wavelengths. After the electric field is obtained by the implicit
 362 solver, we apply the following smoothing operator for each grid node indexed by i, j :

$$\mathbf{E}'_{i,j} = \alpha \mathbf{E}_{i,j} + \frac{1-\alpha}{4} \sum_{4 \text{ neighbors}} \mathbf{E}_{i',j'} \quad (14)$$

363 where the averaging is done over the 4 immediate neighbors of the cell, while in 3D the
 364 averaging is done for 6 neighbors. In most of the presented simulations we use $\alpha = 1/2$
 365 and apply 5 smoothing iterations. In one particular simulation we found that the smooth-
 366 ing caused an instability at the boundary of the PIC domain. To avoid this issue, we have
 367 implemented the option to set $\alpha = 1$ at the few cells near the boundary of the PIC region
 368 (no smoothing) and only apply the smoothing in the inside:

$$\alpha = \min(1, \alpha_0 + (A - \alpha_0) \max(0, 1 - d/D)) \quad (15)$$

369 where α_0 is the internal smoothing parameter, d is the distance of the cell from the bound-
370 ary and A and D are two constants (we use $A = 2$ and $D = 8\Delta x$). For sake of consistency,
371 we also smooth the current densities used in the Maxwell solver. We carefully checked
372 that the overall solution is not affected significantly by the smoothing operation other than
373 eliminating the Langmuir patterns.

374 **5 Two-dimensional Magnetosphere Problem**

375 Our goal is to study the interaction of global and micro scales in a relatively sim-
376 ple system. The two-dimensional (2D) magnetosphere problem [Daldorff *et al.*, 2014] is
377 well-suited: the global scale is set by the interaction of the intrinsic line dipole field and
378 the incoming plasma flow (that we will call the solar wind). A 2D simulation can be run
379 much faster than a 3D problem, so we can do a more extended parameter study. In addi-
380 tion, visualization of the 2D results is much simpler and comprehensive. Of course, the
381 3D reconnection dynamics is somewhat different from the 2D case, but the scaling argu-
382 ments apply to both. For sake of easier interpretation, the values are set to be similar to
383 those typical for Earth's magnetosphere. Note, however, that the 2D simulations are in the
384 magnetic meridional plane, so the Y axis is aligned with the dipole and the Z direction is
385 normal to the plane of the simulation, which is the opposite of the usual 3D case.

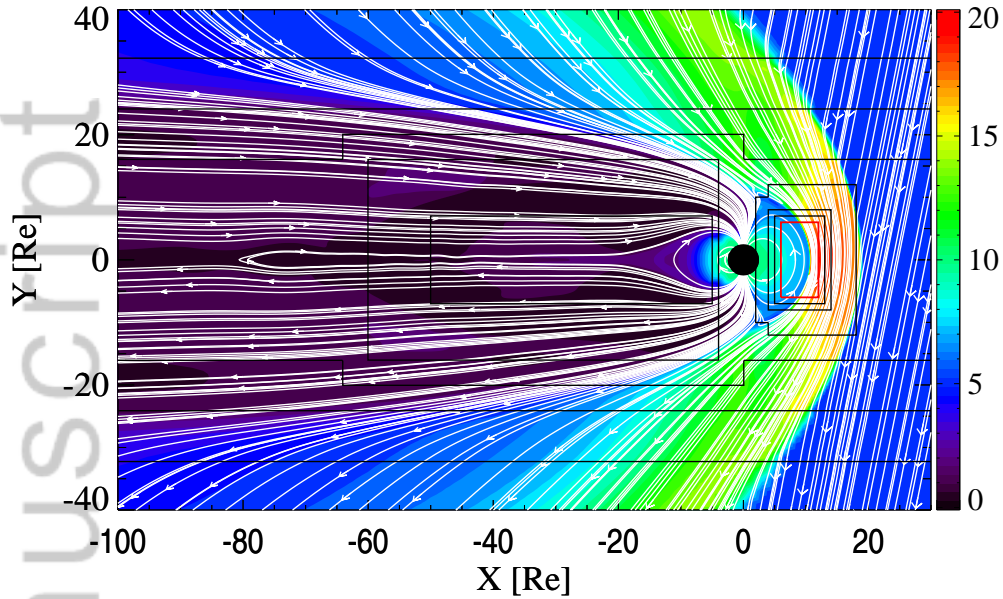
386 The 2D domain extends from $x = -480 R_E$ to $x = 32 R_E$ and $y = -128 R_E$ to
387 $y = 128 R_E$ (where $R_E = 6380$ km is the radius of the Earth) with the magnetized planet
388 at the origin. The inner boundary condition is set at a circle of radius $2.5 R_E$ with a fixed
389 plasma density of 10 amu/cm^3 and zero velocity. The radial component of the magnetic
390 field is set to the line dipole value. The tangential components of the magnetic field and
391 the ion and electron pressures have zero gradient boundary conditions. The line dipole is
392 aligned with the Y axis and its strength is set to $-3,110$ nT at the magnetic equator. This
393 is ten times weaker than the 3D dipole strength of the Earth, but the line dipole field de-
394 cays with r^{-2} instead of the r^{-3} of the 3D dipole, so the magnetopause ends up to be at
395 about the same distance ($10 R_E$) as for Earth's magnetosphere.

396 The solar wind enters from the $+X$ direction with mass density 5 amu/cm^3 , speed
397 -400 km/s, and total pressure 0.031 nPa, of which the electrons have 0.0248 nPa. The
398 electron pressure dominates the pressure of the incoming plasma, but behind the bow
399 shock the ion pressure becomes dominant (by about a factor of 2), because the bow shock

400 is modeled with the MHD code, so the heating of the electrons and ions is determined by
401 the MHD conservation laws. The shock predominantly heats the ions as the bulk kinetic
402 energy is transformed into ion thermal energy (see equations 9 and 13), while the elec-
403 trons only heat up adiabatically according to equation 10.

404 The boundary conditions at $y = \pm 128$ are also set to the fixed solar wind paramete-
405 rs. At this distance the solar wind is only slightly perturbed by the interaction with the
406 magnetosphere, so fixed boundary conditions work well. Finally, a zero gradient outflow
407 boundary condition is applied at $x = -480 R_E$. The outflow boundary has to be placed far
408 away to avoid numerical problems due to the sub-fast magnetosonic flow behind the bow
409 shock.

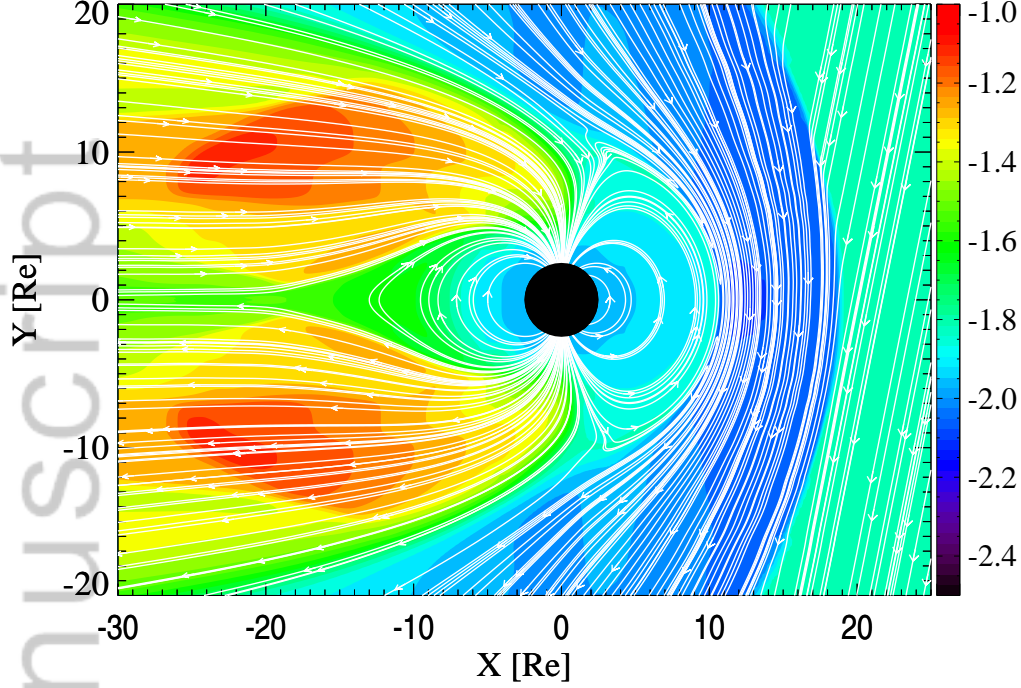
410 The interplanetary magnetic field (IMF) carried by the solar wind is either set to
411 $\mathbf{B} = (-0.1, -0.5, 0)$ nT or $\mathbf{B} = (-0.1, -0.5, -3)$ nT. The Y component is the most important,
412 as it reconnects with the dipole field of the body, which is aligned with the Y axis. In 2D
413 the IMF cannot slip around the magnetosphere, so the magnetic field has to reconnect at
414 the same average rate as it enters into the system. The $B_y = -0.5$ nT value is selected to
415 yield (a slowly decreasing) magnetopause distance at around $10 R_E$. The B_x component
416 is small, but it is set to a non-zero value to break the “north-south” symmetry. If it is set
417 to zero, the Hall MHD simulations produce very large islands at the subsolar point of the
418 magnetopause that can grow to unreasonable size before finally starting to move to the $\pm Y$
419 direction. Finally, the B_z component controls the amount of guide field at the reconnect-
420 tion site. The $B_z = 0$ choice produces pure anti-parallel reconnection with no guide field,
421 while the $B_z = -3$ nT value creates a moderate guide field. Although the IMF magnitude
422 of $|B_z| = 3$ nT is much larger than the IMF magnitude of $|B_y| = 0.5$ nT, near the magne-
423 topause they become comparable. This happens because of the 2D geometry. At the bow
424 shock both components get amplified by the shock compression ratio, which is close to 4
425 for this strong shock, so $|B_y|$ and $|B_z|$ become about 2 nT and 12 nT, respectively. In the
426 magnetosheath, however, $|B_y|$ gets further amplified to about 15 nT due the deceleration in
427 the X direction, while B_z is simply advected around the obstacle. The reason is that the
428 flow deflects from the $-X$ to the $\pm Y$ direction in an approximately incompressible manner,
429 which enhances B_y but not B_z . In the end, the guide field B_z becomes comparable to the
430 reconnecting field B_y on the sheath side of the reconnection.



431 **Figure 1.** Overview of the initial state after the first 10,000 iterations. Only a part of the computational do-
 432 main is shown. The colors show density in units of amu/cm^3 . The white lines are magnetic field lines, while
 433 the black lines represent the grid resolution changes. The red box shows the boundaries of the PIC region.

434 With these parameters, the dayside reconnection site is at the nose of the magne-
 435 topause centered at around $x = 10 R_E$ and $y = 0$ as shown in Figure 1. In BATS-R-
 436 US we solve for the Hall term in the “Hall region” placed at $5 R_E < x < 20 R_E$ and
 437 $-15 R_E < y < +15 R_E$ with a smooth tapering at the edges. Limiting the region where the
 438 Hall term is used improves computational efficiency without any significant effect on the
 439 results around the reconnection site.

440 In the MHD-EPIC simulations, the PIC region (indicated by the red rectangle in
 441 Figure 1) is positioned at $6 R_E < x < 12 R_E$ and $-6 R_E < y < +6 R_E$, which covers the
 442 reconnection site but avoids getting very close either to the body where the plasma beta
 443 is very low, or to the bow shock. Note that the PIC region is fully covered by the Hall
 444 region, so the Hall effect is taken into account on both sides of the boundaries of the PIC
 445 region.



446

Figure 2. The base 10 logarithm of the inertial length measured in R_E for protons.

447

448

449

450

451

452

453

454

To assess the required grid resolution, we plot the base 10 logarithm of the proton ion inertial length $d_{i,p}$ in units of R_E in Figure 2 for the initial conditions. Near the day-side reconnection site $d_{i,p} \approx 0.01 R_E$, which means that $d_e \approx 0.001 R_E$ for the $m_i/m_e = 100$ mass ratio. Resolving the electron scales at least marginally would require $\Delta x \approx d_e$ which would make the PIC region resolved by $6,000 \times 12,000 = 72$ million grid cells and 450 times that many macro-particles, or about 32 billion in total. While this is still doable in 2D, it is a very expensive calculation and in fact the electron scales are still only marginally resolved. In three spatial dimensions things get clearly unfeasible.

455

456

457

458

459

460

Our numerical experiments require that d_i/d_g be a small number, but it is not necessary to start from $d_i = d_{i,p}$ corresponding to $f = 1$. To make the computations affordable, the smallest scaling factor will be set to $f = 8$, which makes $d_i/d_g = f * d_{i,p}/d_g \approx 0.008$, clearly still much less than unity. Correspondingly, the finest grid resolution in the PIC region will be set to $\Delta x = 1/128 R_E$. The corresponding PIC grid is 768×1536 with about 530 million macro-particles.

6 Simulations

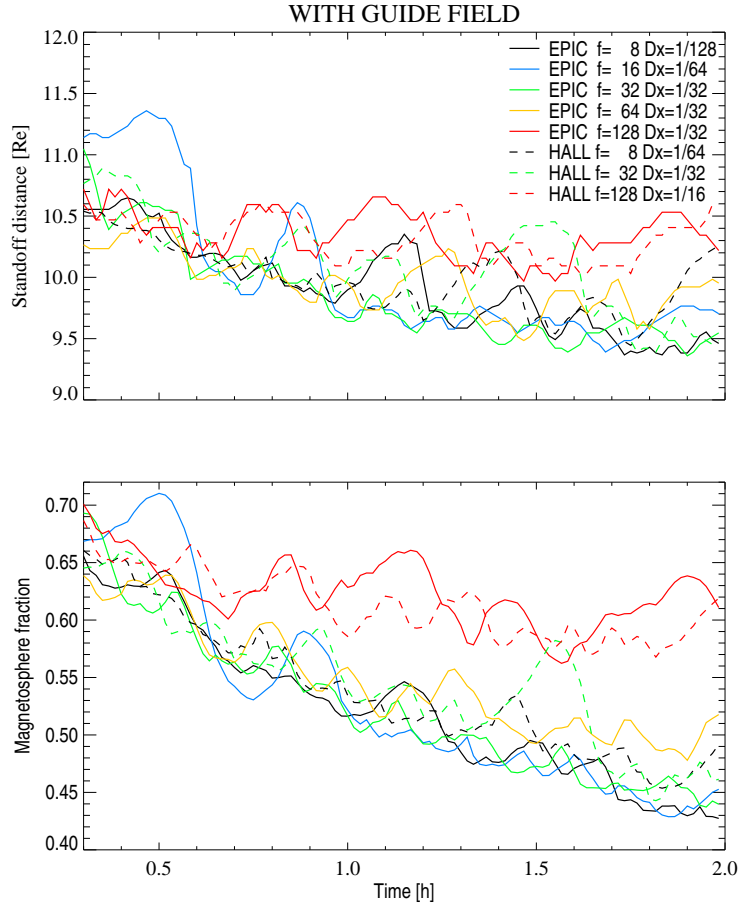
We perform two-fluid and MHD-EPIC simulations with grid resolutions Δx varied from $1/128 R_E$ to $1/16 R_E$ and scaling factors f varied between 8 and 128. For the two-fluid simulations Δx refers to the MHD grid resolution around the reconnection site and f is the ion mass per charge m_i/q_i in the Hall term in Ohm's law (equation 12). In the MHD-EPIC simulations Δx is the grid resolution of the PIC model and f is the scaling factor applied to the ion and electron mass per charge ratios. The only other quantity that is varied is the out-of-plane B_z component of the solar wind that is either 0 (no guide field) or -3 nT (guide field). We will present results from the simulations with the guide field unless otherwise noted.

All simulations are initialized with a steady state solution obtained with the resistive MHD equations, however, the grid resolution around the dayside reconnection site varies from $\Delta x = 1/16$ to $1/128 R_E$, which means that the initial conditions are similar but not necessarily identical. All simulations are run for 2 hours, which is sufficient to reach the quasi-periodic formation of magnetic islands, also called flux transfer events (FTEs).

6.1 Global scales

One of the most characteristic length scales of a magnetosphere is the standoff distance. This is usually estimated to be a position along the $+X$ axis where the magnetic pressure of the (compressed) dipole field balances the ram pressure of the solar wind. The issue is more complicated in 2 spatial dimensions, because the Y component of the magnetic field entering with the solar wind has no other way to get to the other side of the planet than magnetic reconnection. If the reconnection rate is too slow, the field will pile up outside the magnetopause. If the reconnection rate is too fast, it will erode the magnetopause too quickly.

We selected the line dipole strength and B_Y to form a magnetopause with about the same standoff distance as found in Earth's 3D magnetosphere. During the time dependent simulation the standoff distance is slowly decreasing on average. In addition, there are oscillations related to the large scale dynamics of the reconnection process. Comparing the time variation of the standoff distance for the simulations using different kinetic scaling factors provides a simple quantitative assessment of their similarities and differences. We use the following simple formula to calculate the standoff distance automatically from the



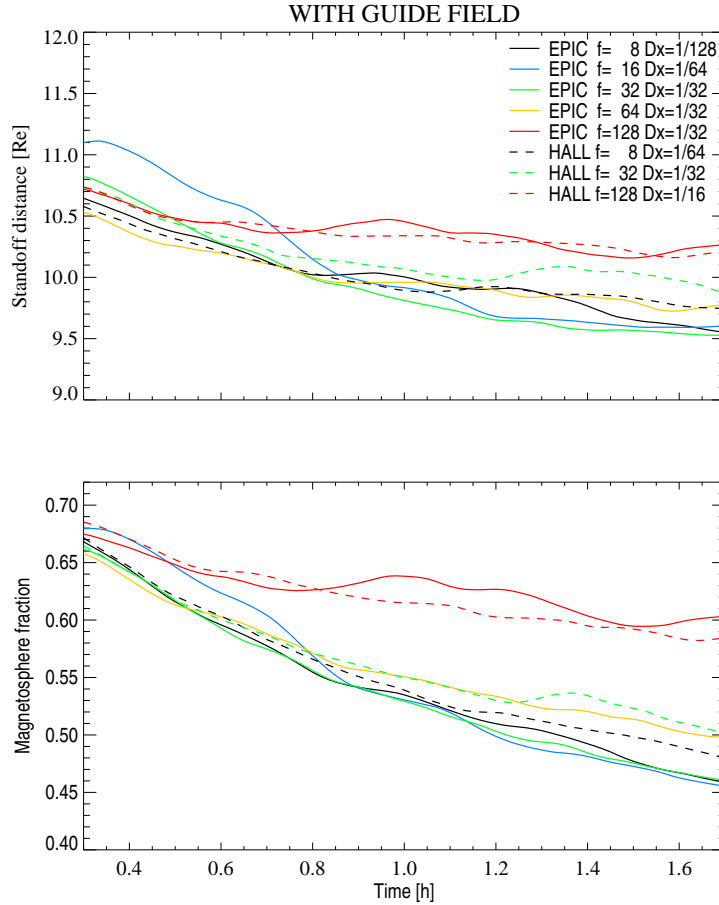
477 **Figure 3.** Time series of the standoff distance and the volume fraction of the magnetosphere inside the
 478 PIC region for several MHD-EPIC and Hall MHD simulations. The kinetic scaling factors (f) and the grid
 479 resolutions (Dx) are indicated in the figure legend. All simulations used IMF $B_Z = -3$ nT.

498 solution on the discrete grid:

$$S = \max_{\{i,j: B_{Y,ij} > 3 \text{ nT}\}} x_{ij} \quad (16)$$

499 where i, j are the indexes of the grid cells. This works well, since $B_Y < 0$ in the solar
 500 wind and behind the bow shock, and it is positive inside the magnetopause near the sub-
 501 solar point. The threshold value of 3 nT was selected so that small B_Y perturbations up-
 502 stream of the magnetopause are ignored.

503 Another simple measure for the size of the dayside magnetosphere is the fraction of
 504 volume where B_Y is positive around the dayside magnetopause. For the sake of simplicity
 505 we use the grid cells inside the PIC region ($6 R_E < x < 12 R_E$ and $-6 R_E < y < 6 R_E$) and



480 **Figure 4.** Time series of the standoff distance and the volume fraction of the PIC region occupied by mag-
 481 netospheric plasma for several MHD-EPIC and Hall MHD simulations smoothed with a 30-minute boxcar
 482 averaging. The simulations used IMF $B_Z = -3$ nT.

506 define

$$F = \frac{1}{A} \sum_{\{i,j: B_{Y,ij} > 3 \text{ nT}\}} \Delta A_{ij} \quad (17)$$

507 where ΔA is the size of the grid cell and $A = 72 R_E^2$ is the total area of the region. This
 508 measure is less sensitive to the local variations than the standoff distance, but for the sake
 509 of simplicity we use the same threshold value 3 nT.

510 Figures 3 and 4 show the time series of the standoff distance S and the volume frac-
 511 tion of the magnetosphere inside the PIC region F . Figure 3 provides the values with a
 512 1-minute cadence between $t = 0.3$ and $t = 2$ hours. Figure 4 shows the same quantities
 513 smoothed with a 30-minute wide boxcar averaging. Both quantities get smaller with time,

514 which means that the reconnection is eroding the magnetopause and the magnetosphere
515 slowly shrinks. Simulations with $f = 128$ are clearly different from the others in both fig-
516 ures. This is expected, since in this case the separation of kinetic and global scales is not
517 large anymore: $\varepsilon = f d_{i,p}/d_g \approx 128 * 0.01/10 = 0.128$.

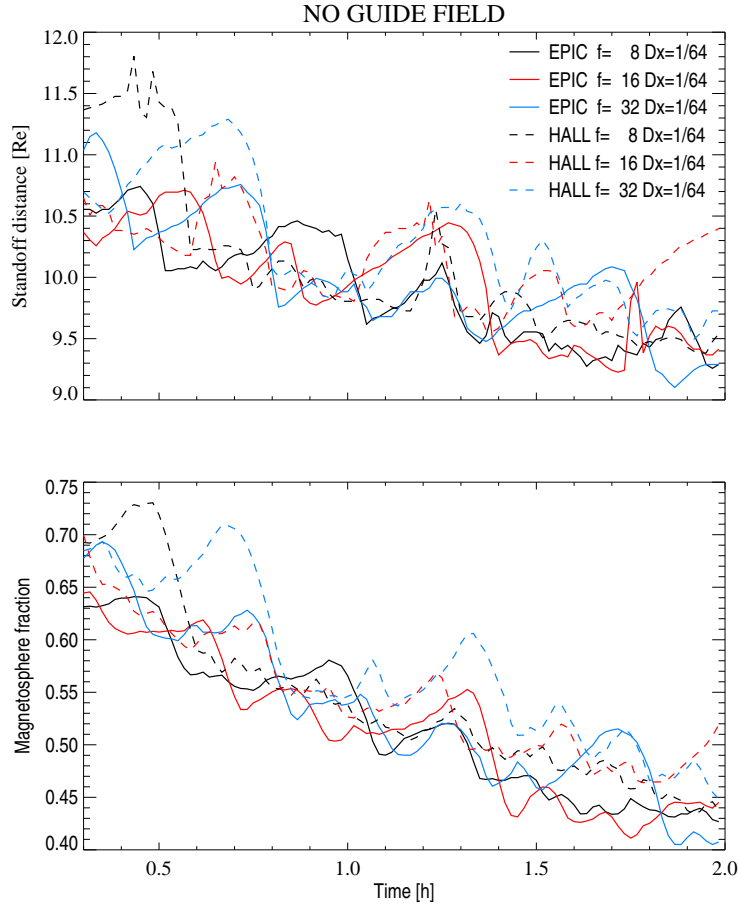
518 At first glance, the rest of the simulations with $f \leq 64$ look similar when the un-
519 smoothed curves are compared. The smoothed magnetosphere fraction curves (bottom
520 panel of Figure 4), however, clearly reveal that the Hall MHD simulations (dashed lines)
521 and the MHD-EPIC simulation with $f = 64$ (orange line) significantly deviate from the
522 three MHD-EPIC simulations with $f = 8, 16$ and 32 (black, cyan and green solid lines)
523 which are quite similar to each other overall.

524 The standoff distance varies more, even with smoothing (top panel of Figure 4), but
525 the trends are the same: the MHD-EPIC simulations with kinetic scaling factor $f \leq 32$ are
526 closer to each other than the rest of the simulations.

533 Figures 5 and 6 show results from several simulations with no guide field, i.e. the
534 IMF $B_Z = 0$. In these simulations the grid resolution is kept constant at $\Delta x = 1/64 R_E$
535 while the kinetic scaling factor is varied between 8 and 32, so all simulations start from
536 the same initial condition. The standoff distance and the magnetosphere fraction without
537 smoothing and with 30-minute boxcar smoothing are shown in the figures, respectively.

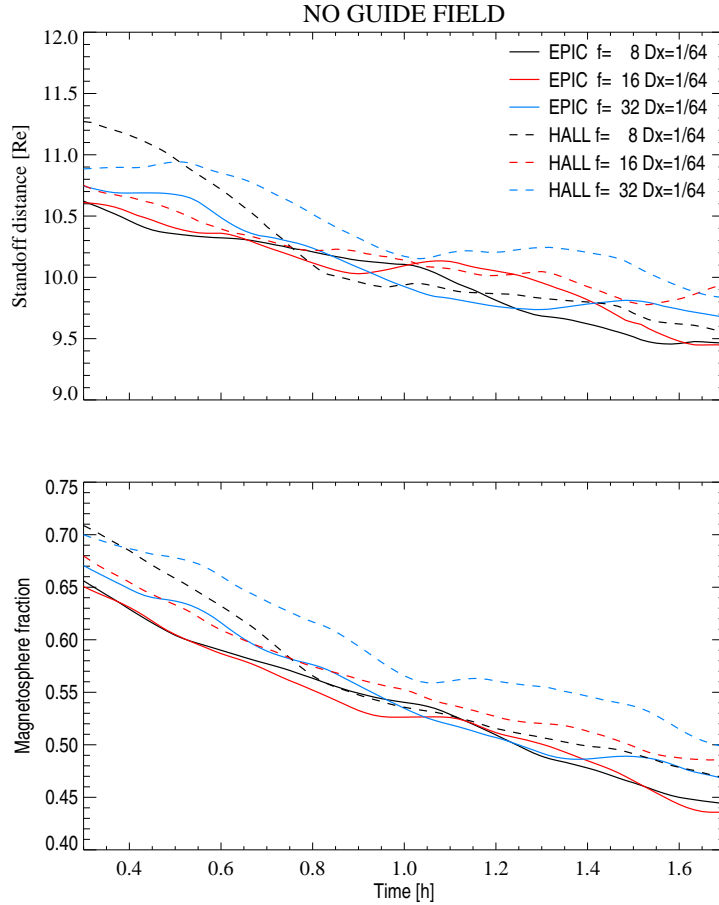
538 Overall, the decay rates of the standoff distances are similar, but the Hall MHD sim-
539 ulations show some sharp spikes corresponding to $B_y > 3$ nT spots produced by very large
540 FTEs. In contrast the MHD-EPIC simulations show less variation. The volume fraction
541 of the magnetosphere shows smoother variation, as expected. Still, it is clear that the Hall
542 MHD simulations show larger oscillations than the MHD-EPIC solutions. The smoothed
543 curves on Figure 6 show similar trends for all six simulations, although both the standoff
544 distance and the magnetosphere fraction is somewhat larger for the Hall MHD simulations
545 (dashed curves) than for MHD-EPIC (solid curves).

550 We now focus on the phenomena causing the fluctuations: the large scale magnetic
551 islands, or FTEs. Figure 7 compares FTEs produced by two MHD-EPIC runs. The simu-
552 lation shown on the left uses $f = 8$ for the kinetic scaling factor with a $\Delta x = 1/128 R_E$
553 grid resolution in the PIC domain, while the one on the right uses $f = 32$ and $\Delta x =$
554 $1/32 R_E$. The three rows correspond to times separated by 3 minutes. The initial times



527 **Figure 5.** Time series of the standoff distance and the volume fraction of the PIC region occupied by
 528 magnetospheric plasma for several MHD-EPIC and Hall MHD simulations. There is no guide field: IMF
 529 $B_Z = 0$.

555 (29 and 55 minutes, respectively) are selected so that the FTEs moving towards the $+Y$ di-
 556 rection are roughly at the same stage of evolution. In the top row the center of the FTEs
 557 are roughly at $Y = 3 R_E$, then 3 minutes later (middle row) they get to about $Y = 5 R_E$
 558 and another 3 minutes later (bottom row) the centers move to about $Y = 8 R_E$. Over-
 559 all the size and shape of these flux ropes are very similar. The propagation speed in the
 560 Y direction is about $2 R_E/3 \text{ min} \approx 71 \text{ km/s}$ between the initial and midpoint times, and
 561 $3 R_E/3 \text{ min} \approx 106 \text{ km/s}$ between the midpoint and final times. These velocities are close to
 562 the Y component of the plasma velocity shown by the colors in the figure.



530 **Figure 6.** Time series of the standoff distance and the volume fraction of the PIC region occupied by mag-
 531 netospheric plasma for several MHD-EPIC and Hall MHD simulations smoothed with a 30-minute boxcar
 532 averaging. There is no guide field: IMF $B_Z = 0$.

563 The fluxropes moving in the $-Y$ direction also show similar sizes and shapes, al-
 564 though at this particular time there are multiple flux ropes on the left, and only one dom-
 565 inant flux rope on the right, so their evolution is different. The total number and size dis-
 566 tribution of flux ropes is also very similar. Looking at animations of multiple simulations
 567 side by side indicates that the large scale FTE dynamics is quite insensitive to the value of
 568 the scaling factor f .

6.2 Kinetic scales

Figure 8 shows the simulation result near the dayside reconnection sites in three simulations with different scaling factors and grid resolutions. The times shown are selected so that the reconnection sites are near the subsolar point of the magnetopause. The Y component of the electron velocity (left column) shows the reconnection jets, while the Z (out-of-plane) component of the electron and ion velocities (middle and right columns) show the current carried by the electrons and ions, respectively. Although the three reconnection sites are from different simulations at different times, the similarities are quite clear. The two simulations with $f = 32$ (middle and bottom rows) are on the same spatial scale, but the grid resolutions are a factor of 4 different. Still, the width of the current sheet near the reconnection site, as indicated by the maxima (red color) of the Z component of the electron velocity are quite similar, around $0.1 R_E$ or about 3 to 4 d_e , where the electron skin depth is measured on the sheath side of the reconnection site. The width of the ion diffusion regions (shown by the blue regions in the right column) is about $1 R_E$ wide in both cases, which is 10 times wider than the electron diffusion region as expected for the $m_i/m_e = 100$ mass ratio. The electron exhaust jets (left column), although different in detail, also show similar spatial structures and the exhaust velocities have similar values. This suggests that the reconnection dynamics is not dominated by grid resolution effects.

The spatial scales shown for $f = 8$ (top row) are 4 times smaller than the spatial scales shown for the two simulations with $f = 32$. After this visual rescaling the solutions look remarkably similar. The width of the current sheet near the reconnection site (red area in the top middle panel) is about $0.025 R_E$ that is indeed 4 times thinner than the current sheets obtained with $f = 32$. The width of the ion diffusion region (blue region in the top right panel) also scales approximately with f . The overall structure and velocity of the reconnection jets is also similar (left column) after the spatial rescaling. These results support the arguments made in subsection 2.2: the kinetic scales are proportional to f .

In contrast to the PIC solution, in Hall MHD there is no electron scale, so the solution depends, to some extent, on the grid resolution, which determines the numerical dissipation. Figure 9 demonstrates this by comparing two Hall MHD simulations that used the same kinetic scaling factor but grid resolutions differing by a factor of four. The snapshots are selected to capture magnetic islands of similar sizes and shapes at the same location

609 and time ($t = 76$ min) in the two simulations. While the qualitative pictures are similar,
610 and in fact the magnetic fields are very comparable, there are significant quantitative dif-
611 ferences. In Hall MHD the width of the current sheet is determined by the grid resolution,
612 so it is much thinner on the $\Delta x = 1/128 R_E$ grid than on the $\Delta x = 1/32 R_E$ grid. Con-
613 sequently, the out-of-plane component of the current (determined from $\nabla \times \mathbf{B}$) is much
614 stronger for the higher resolution run.

615 **6.3 Intermediate scales**

621 We argued in subsection 2.3 that the solution should be self-similar at the interme-
622 diate scales. Indeed, Figure 10 demonstrates that the growth of an FTE is approximately
623 self-similar. The top and bottom rows show the same FTE at two different times. The
624 panel sizes are $0.7 \times 1.5 R_E$ for time $t = 16$ m and $1.4 \times 3 R_E$ for $t = 20$ m. The simula-
625 tion uses $f = 8$ for the scaling factor, so the kinetic scales are quite small ($d_i \approx 0.08 R_E$).
626 The grid resolution is $\Delta x = 1/128 R_E$, so the intermediate and global scales are very
627 well resolved. The FTE was selected based on its formation near the sub-solar point, so it
628 stayed roughly at the same place while growing in size. The quantities shown are electron
629 pressure, the out-of-plane component of the electron velocity and the Y component of the
630 magnetic field. We checked that all other quantities show the same behavior.

631 Comparing the solution at these two times demonstrates that the evolution of an iso-
632 lated FTE is approximately self-similar at the intermediate scales, which supports our the-
633 oretical arguments presented in subsection 2.3.

634 **7 Conclusions**

635 In many space plasma systems global and kinetic scales are separated by many or-
636 ders of magnitude, nevertheless the global system has a major influence on the kinetic
637 processes, and vice versa, the kinetic processes, especially magnetic reconnection, has a
638 major impact on the global dynamics. This scale separation presents a challenge to theo-
639 retical, observational and modeling investigations. The kinetic scales, such as the Debye
640 length, electron skin depth, electron gyro radius, ion inertial length and ion gyro radius
641 are all proportional to the mass to charge ratio of electrons and ions. We showed that one
642 can artificially change the kinetic scales by changing the ion and electron mass to charge

643 ratios by a scaling factor f while keeping the MHD quantities, such as mass density, pres-
644 sure, bulk velocity and magnetic field the same.

645 We presented a number of theoretical arguments suggesting that as long as the sepa-
646 ration between global and kinetic scales remains large enough:

- 647 1. The solution of the equations is insensitive to the scaling at global scales.
- 648 2. The solution at kinetic scales will look the same but spatially proportional to the
649 scaling factor.

650 Our numerical experiments conducted with the MHD-EPIC code show not only that these
651 theoretical expectations are fulfilled, but also that the required separation of scales is rela-
652 tively modest. For the dayside reconnection process the global scale can be characterized
653 by the magnetopause stand-off distance that is $d_g \approx 10 R_E$. We found that scaling factors
654 $f \leq 32$ corresponding to the scaled inertial length $d_i \leq 0.32 R_E$ and $\varepsilon = d_i/d_g \leq 0.032$
655 give very comparable solutions. Further increasing the ion inertial length to $d_i \geq 0.64 R_E$
656 and $\varepsilon \geq 0.064$, however, produces significantly different results. The simulations also con-
657 firmed that the scaled MHD-EPIC simulations provide very similar solutions at the kinetic
658 scales when distance is measured in the ion inertial length d_i that is proportional to the
659 scaling factor f .

660 In principle the scaling arguments apply to Hall MHD as well, but in this case the
661 electron scale processes are replaced by numerical and/or some ad hoc resistivity. Assum-
662 ing that these resistive effects are kept proportional to the grid resolution Δx in a Hall
663 MHD simulation, one would expect that keeping the ratio $d_i/\Delta x$ constant and/or very
664 large is analogous to keeping $d_i/d_e = \sqrt{m_i/m_e}$ constant and/or large in the PIC simula-
665 tions. Our results suggest that this is approximately true, so Hall MHD simulations can
666 also benefit from the kinetic scaling. We expect that the same is true for hybrid simula-
667 tions that include the Hall effect.

668 The scaling of kinetic effects is interesting from a theoretical point of view. The
669 scaling reduces the number of free parameters that enter the system, therefore results ob-
670 tained for a given inertial length will have more general applicability. In addition, the scal-
671 ing and self-similarity may provide insight into the generic properties of collisionless re-
672 connection: distribution of magnetic island sizes, for example, is likely to follow some
673 power laws. Investigating these theoretical consequences is left for future work.

674 The scaling also has a very practical application, which in fact motivated our re-
675 search in the first place: increasing the ion inertial length makes kinetic simulations em-
676 bedded into a global system possible. Resolving the real ion inertial length in three-dimensional
677 simulations of Earth's magnetosphere is extremely difficult even on the largest available
678 computers. Doing the same in the solar corona is essentially hopeless. To put some num-
679 bers behind these statements, let us consider a 3D global magnetosphere simulation box of
680 $100 \times 100 \times 100 R_E^3$. An explicit kinetic simulation has to resolve the Debye length that is
681 about 100 meters or $\Delta x = 1/64000 R_E$. The required number of grid cells would be order
682 3×10^{20} , the number of macroparticles would be about 10^{23} and the time step would be
683 limited to $\Delta x/c = 0.3$ microseconds. Doing one hour of simulation would require 10^{33}
684 particle pushes. Each particle push requires order of 100 floating point operations (includ-
685 ing the interpolation of the fields to the particle positions), so even on a future exascale
686 computer which can do 10^{18} operations per second, this single simulation would take 10^{17}
687 seconds wall clock time or about 3 billion years. Clearly, waiting for faster computers will
688 not make such a simulation possible. One can switch to an implicit PIC code that requires
689 resolving the electron skin depth (instead of the Debye length) that is about 1.5 km and
690 the time step is restricted by the cell crossing time at the electron thermal speed instead of
691 the speed of light. Reducing the ion-electron mass ratio from 1836 to 100 results in an-
692 other factor of ≈ 4 increase in the cell size to $\Delta x = 6 \text{ km} \approx 1/1000 R_E$, while the time
693 step increases by a factor of about 6000 relative to the explicit PIC code with realistic
694 electron mass to $\Delta t \approx 2$ milliseconds, which in turn reduces the computational cost by a
695 factor of 10^9 to 3 years on the future exascale machine. The MHD-EPIC algorithm allows
696 restricting the PIC code to the vicinity of the reconnection region(s), while one can use
697 an adaptive grid for the global MHD code. The speed up is approximately the ratio of the
698 volume of the PIC region relative to the whole domain, which is about 10^3 . This reduces
699 the computational cost to 1 day on a future exascale computer, which is promising, or
700 about 3 years on a current petascale machine, still out of reach for now. With the kinetic
701 scaling presented in this paper, however, the simulation becomes feasible. Using a scaling
702 factor $f = 32$ allows 32 times coarser grid size of about $\Delta x = 200 \text{ km} = 1/32 R_E$ and 32
703 times larger time step $\Delta t \approx 0.06$ second. This saves $f^4 \approx 10^6$, which makes the simulation
704 doable in a few days using a few thousand cores (instead of a full petascale machine) with
705 a code that in practice can only achieve a fraction of the peak performance. Our compan-
706 ion paper by *Chen et al.* [2017, accepted companion paper] does in fact present a 1-hour

707 long 3D magnetosphere simulation using the MHD-EPIC model with kinetic scaling that
708 was obtained with 6400 cores of the Blue Waters computer running for a week.

709 In general, with proper kinetic scaling, the cost of the computation depends on the
710 smallest global scales rather than on the true kinetic scales. Our simulations suggested
711 that one can get reasonably accurate results with a scaled up inertial length d_i that is
712 about 3% of the global scale d_g . Resolving the increased ion inertial length scale requires
713 a grid resolution $\Delta x \approx d_i/10 \approx d_g/300$. This is much finer than the typical grids used in
714 global MHD simulations that typically resolve the global scale with order 20 to 50 cells,
715 but still achievable on current computers. Roughly speaking, kinetic simulations will re-
716 quire a grid resolution that is about 10 times finer than the grids used in MHD simula-
717 tions, and the time step will also be about 10 times smaller. The computational cost of a
718 3D simulation is proportional to $\Delta x^{-3} \Delta t^{-1}$, so this a factor of 10,000 increase. In two spa-
719 tial dimensions the cost is proportional to the 3rd power, or about factor of 1000. In addi-
720 tion, kinetic simulations are more expensive than MHD simulations on the same grid. The
721 use of adaptive mesh refinement can reduce this cost substantially, because the high reso-
722 lution is only needed in a relatively small region. Further efficiency gain can be achieved
723 by using the MHD-EPIC algorithm, so that the PIC model is limited to the vicinity of the
724 reconnection site. In summary, even with the scaling, kinetic simulations are much more
725 expensive than ideal or resistive MHD simulations, but much more affordable than trying
726 to resolve the true kinetic scales that may be many orders of magnitude smaller.

727 In contrast with pure MHD or pure PIC models, the MHD-EPIC approach combined
728 with the kinetic scaling allows studying

- 729 1. kinetic dynamics embedded into a realistic and possibly time-dependent global en-
730 vironment, and
- 731 2. the self-consistent feedback of the kinetic solution on the global dynamics.

732 Studying collisionless reconnection in global systems allows, for example, direct compar-
733 ison of full electron and ion distribution functions with observations, such as those pro-
734 vided by the MMS mission. Self-consistent MHD-EPIC simulations can get correct colli-
735 sionless reconnection rates and global dynamics based on electron physics instead of nu-
736 merical resistivity. This may lead to a better understanding of the mechanisms producing
737 magnetospheric substorms and solar eruptions, for example.

738 This paper focused on the kinetic scaling and demonstrated it with 2D simulations.
739 We have already performed 3D MHD-EPIC simulations for Earth's magnetosphere using
740 scaling factors $f = 16$ and $f = 32$. The results of these simulations are discussed in an
741 accompanying paper by *Chen et al.* [2017, accepted companion paper] showing several ki-
742 netic effects predicted and observed in the dayside magnetosphere including flux transfer
743 events, Larmor electric field, the lower hybrid drift instability (LHDI) and crescent shape
744 velocity distribution functions. Our 2D and 3D simulations focused on various aspects
745 of the reconnection process at the dayside magnetopause and found that the kinetic scal-
746 ing works for these. It will require further research to examine if these results generalize
747 to other aspects (like particle acceleration), other parameter regimes (reconnection in so-
748 lar flares) and other type of kinetic processes (for example kinetic instabilities at parallel
749 shocks).

750 **Acknowledgments**

751 This research was partially supported by INSPIRE NSF grant PHY-1513379, by the NSF/NASA
752 LWS Strategic Capabilities grant AGS-1322543, and by the Space Hazards Induced near
753 Earth by Large, Dynamic Storms (SHIELDS) and the Impacts of Extreme Space Weather
754 Events on Power Grid Infrastructure projects funded by the U.S. Department of Energy
755 (DE-AC52-06NA25396) through the Los Alamos National Laboratory Directed Research
756 and Development program. Paul Cassak was supported by NASA Grant NNX16AF75G.

757 Computational resources supporting this work were provided on the Blue Waters su-
758 per computer by the NSF PRAC grant ACI-1640510, on the Pleiades computer by NASA
759 High-End Computing (HEC) Program through the NASA Advanced Supercomputing
760 (NAS) Division at Ames Research Center, and from Yellowstone (ark:/85065/d7wd3xhc)
761 provided by NCAR's Computational and Information Systems Laboratory, sponsored by
762 the National Science Foundation.

763 The SWMF code (including BATS-R-US and iPIC3D) is publicly available through
764 the csem.engin.umich.edu/tools/swmf web site after registration. The output of the simula-
765 tions presented in this paper can be obtained by contacting the first author GT.

References

- Birn, J., J. F. Drake, M. A. Shay, B. N. Rogers, R. E. Denton, M. Hesse, M. Kuznetsova, Z. W. Ma, A. Bhattacharjee, A. Otto, and P. L. Pritchett (2001), Geospace Environmental Modeling (GEM) magnetic reconnection challenge, *J. Geophys. Res.*, *106*(A3), 3715–3720, doi:10.1029/1999JA900449.
- Boris, J. P. (1970), A physically motivated solution of the Alfvén problem, *Tech. Rep. NRL Memorandum Report 2167*, Naval Research Laboratory, Washington, D.C.
- Brackbill, J., and D. Forslund (1982), An implicit method for electromagnetic plasma simulation in two dimensions, *J. Comput. Phys.*, *46*, 271–308, doi:10.1016/0021-9991(82)90016-X.
- Cassak, P. A., and M. A. Shay (2007), Scaling of asymmetric magnetic reconnection: General theory and collisional simulations, *Phys. Plasmas*, *14*, 102,114, doi:10.1063/1.2795630.
- Chen, Y., G. Tóth, P. Cassak, X. Jia, T. I. Gombosi, J. Slavin, S. Markidis, and B. Peng (2017, submitted companion paper), Global three-dimensional simulation of earth’s dayside reconnection using a two-way coupled magnetohydrodynamics with embedded particle-in-cell model: initial results, *J. Geophys. Res.*
- Daldorff, L. K. S., G. Tóth, T. I. Gombosi, G. Lapenta, J. Amaya, S. Markidis, and J. U. Brackbill (2014), Two-way coupling of a global Hall magnetohydrodynamics model with a local implicit Particle-in-Cell model, *J. Comput. Phys.*, *268*, 236, doi:10.1016/j.jcp.2014.03.009.
- Dedner, A., F. Kemm, D. Kröner, C. Munz, T. Schnitzer, and M. Wesenberg (2003), Hyperbolic divergence cleaning for the MHD equations, *J. Comput. Phys.*, *175*, 645–673.
- Dorelli, J. C., A. Glocer, G. Collinson, and G. Toth (2015), The role of the hall effect in the global structure and dynamics of planetary magnetospheres: Ganymede as a case study, *JGR*, *120*, 5377–5392, doi:10.1002/2014JA020951.
- Gombosi, T. I., G. Tóth, D. L. De Zeeuw, K. C. Hansen, K. Kabin, and K. G. Powell (2002), Semirelativistic magnetohydrodynamics and physics-based convergence acceleration, *J. Comput. Phys.*, *177*, 176–205, doi:10.1006/jcph.2002.7009.
- Hesse, M., K. Schindler, J. Birn, and M. Kuznetsova (1999), The diffusion region in collisionless magnetic reconnection, *Phys. Plasmas*, *6*, 1781, doi:10.1063/1.873436.
- Huba, D., and L. Rudakov (2004), Hall magnetic reconnection rate, *Phys. Rev. Lett.*, *93*, 175,003, doi:10.1103/PhysRevLett.93.175003.

799 Koren, B. (1993), A robust upwind discretisation method for advection, diffusion and
800 source terms, in *Numerical Methods for Advection-Diffusion Problems*, edited by
801 C. Vreugdenhil and B.Koren, p. 117, Vieweg, Braunschweig.

802 Lapenta, G., S. Markidis, A. Divin, M. Goldman, and D. Newman (2010), Scales of guide
803 field reconnection at the hydrogen mass ratio, *Physics of Plasmas*, 17(8), 082,106, doi:
804 10.1063/1.3467503.

805 Liu, Y.-H., M. Hesse, F. Guo, W. Daughton, H. Li, P. A. Cassak, and M. A. Shay (2017),
806 Why does steady-state magnetic reconnection have a maximum local rate of order 0.1?,
807 *Phys. Rev. Lett.*, 118, 085,101, doi:10.1103/PhysRevLett.118.085101.

808 Markidis, S., G. Lapenta, and Rizwan-Uddin (2010), Multi-scale simulations of
809 plasma with ipic3d, *Mathematics and Computers in Simulation*, 80, 1509–1519, doi:
810 10.1016/j.matcom.2009.08.038.

811 Mozer, F. S., and A. Hull (2010), Scaling the energy conversion rate from magnetic field
812 reconnection to different bodies, *Phys. Plasmas*, 17, 102,906, doi:10.1063/1.3504224.

813 Nitta, S., S. Tanuma, and K. Maezawa (2002), A self-similar solution of magnetic re-
814 connection: a semi-analytic study of the inflow region, *Astrophys. J.*, 580, 538, doi:
815 10.1086/343067.

816 Powell, K., P. Roe, T. Linde, T. Gombosi, and D. L. De Zeeuw (1999), A solution-
817 adaptive upwind scheme for ideal magnetohydrodynamics, *J. Comput. Phys.*, 154, 284–
818 309, doi:10.1006/jcph.1999.6299.

819 Powell, K. G. (1994), An approximate Riemann solver for magnetohydrodynamics (that
820 works in more than one dimension), *Tech. Rep. 94-24*, Inst. for Comput. Appl. in Sci.
821 and Eng., NASA Langley Space Flight Center, Hampton, Va.

822 Ricci, P., J. U. Brackbill, W. Daughton, and G. Lapenta (2004), Collisionless magnetic
823 reconnection in the presence of a guide field, *Phys. Plasmas*, 11, 4102.

824 Rusanov, V. (1961), Calculation of interaction of non-steady shock waves with obstacles,
825 *J. Comp. Math. and Phys.*, 1, 267.

826 Schoeffler, K. M., J. F. Drake, and M. Swisdak (2012), Scaling of the growth rate of
827 magnetic islands in the heliosheath, *Astrophys. J. Lett.*, 750(2), L30, doi:10.1088/2041-
828 8205/750/2/L30.

829 Shay, M., J. Drake, B. Rogers, and R. Denton (1999), The scaling of collision-
830 less, magnetic reconnection for large systems, *Geophys. Res. Lett.*, 26, 2163, doi:
831 10.1029/1999GL900481.

832 Shay, M. A., and J. F. Drake (1998), The role of electron dissipation on the rate
833 of collisionless magnetic reconnection, *Geophys. Res. Lett.*, *25*, 3759, doi:
834 10.1029/1998GL900036.

835 Shay, M. A., J. F. Drake, and M. Swisdak (2007), Two-scale structure of the electron dis-
836 sipation region during collisionless magnetic reconnection, *Phys. Rev. Lett.*, *99*, 155,002,
837 doi:10.1103/PhysRevLett.99.155002.

838 Shibata, K., and S. Tanuma (2001), Plasmoid-induced-reconnection and fractal reconnect-
839 tion, *Earth, Planets and Space*, *53*, 473, doi:10.1186/BF03353258.

840 Tenerani, A., M. Velli, A. F. Rappazzo, and F. Pucci (2015), Magnetic reconnection: Re-
841 cursive current sheet collapse triggered by "ideal" tearing, *Astrophys. J. Lett.*, *813*, L32,
842 doi:10.1088/2041-8205/813/2/L32.

843 Tóth, G., I. V. Sokolov, T. I. Gombosi, D. R. Chesney, C. Clauer, D. L. D. Zeeuw, K. C.
844 Hansen, K. J. Kane, W. B. Manchester, K. G. Powell, A. J. Ridley, I. I. Roussev, Q. F.
845 Stout, O. Volberg, R. A. Wolf, S. Sazykin, A. Chan, B. Yu, and J. Kóta (2005), Space
846 Weather Modeling Framework: A new tool for the space science community, *J. Geo-*
847 *phys. Res.*, *110*, A12,226, doi:10.1029/2005JA011126.

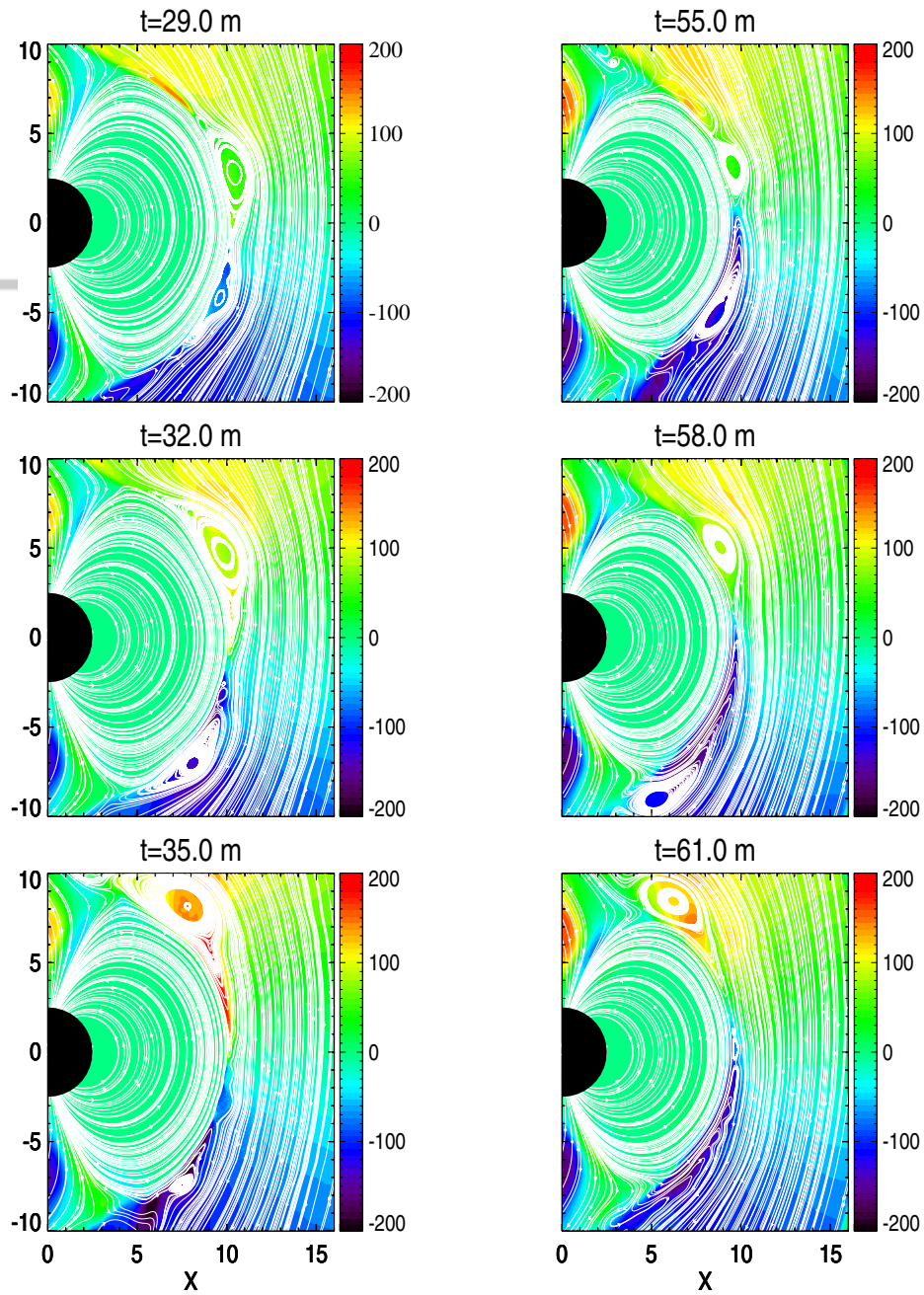
848 Tóth, G., Y. J. Ma, and T. I. Gombosi (2008), Hall magnetohydrodynamics on block adap-
849 tive grids, *J. Comput. Phys.*, *227*, 6967–6984, doi:10.1016/j.jcp.2008.04.010.

850 Tóth, G., B. van der Holst, I. V. Sokolov, D. L. D. Zeeuw, T. I. Gombosi, F. Fang, W. B.
851 Manchester, X. Meng, D. Najib, K. G. Powell, Q. F. Stout, A. Glocer, Y.-J. Ma, and
852 M. Opher (2012), Adaptive numerical algorithms in space weather modeling, *J. Comput.*
853 *Phys.*, *231*, 870–903, doi:10.1016/j.jcp.2011.02.006.

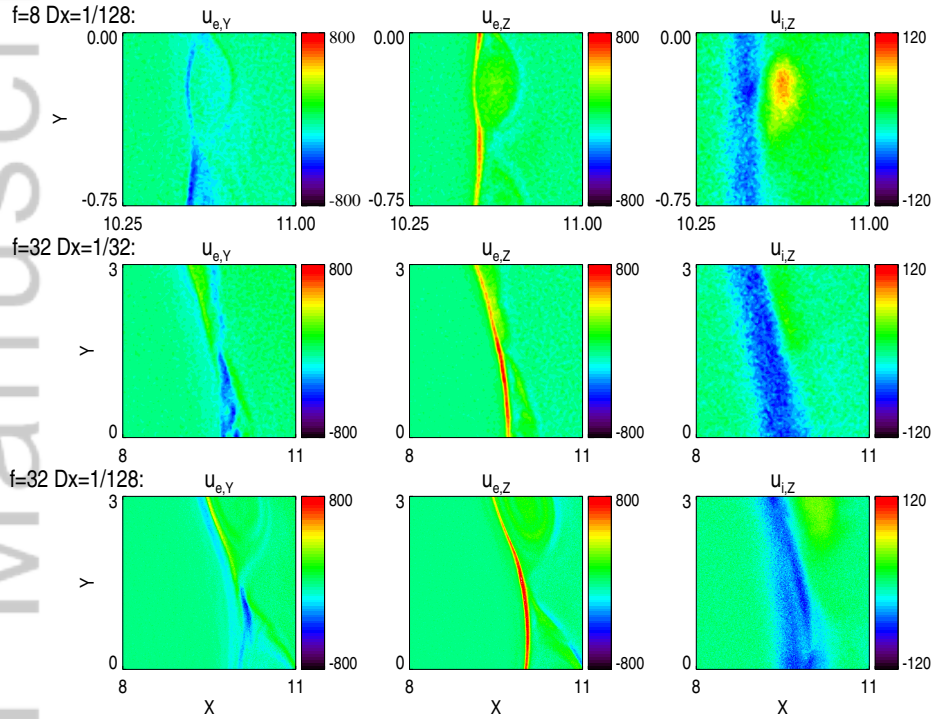
854 Tóth, G., X. Jia, S. Markidis, B. Peng, Y. Chen, L. Daldorff, V. Tenishev, D. Borovikov,
855 J. Haiducek, T. Gombosi, A. Glocer, and J. Dorelli (2016), Extended magnetohydro-
856 dynamics with embedded particle-in-cell simulation of ganymede's magnetosphere, *J.*
857 *Geophys. Res.*, *121*, doi:10.1002/2015JA021997.

858 van Leer, B. (1979), Towards the ultimate conservative difference scheme. V. A second-
859 order sequel to Godunov's method, *J. Comput. Phys.*, *32*, 101–136.

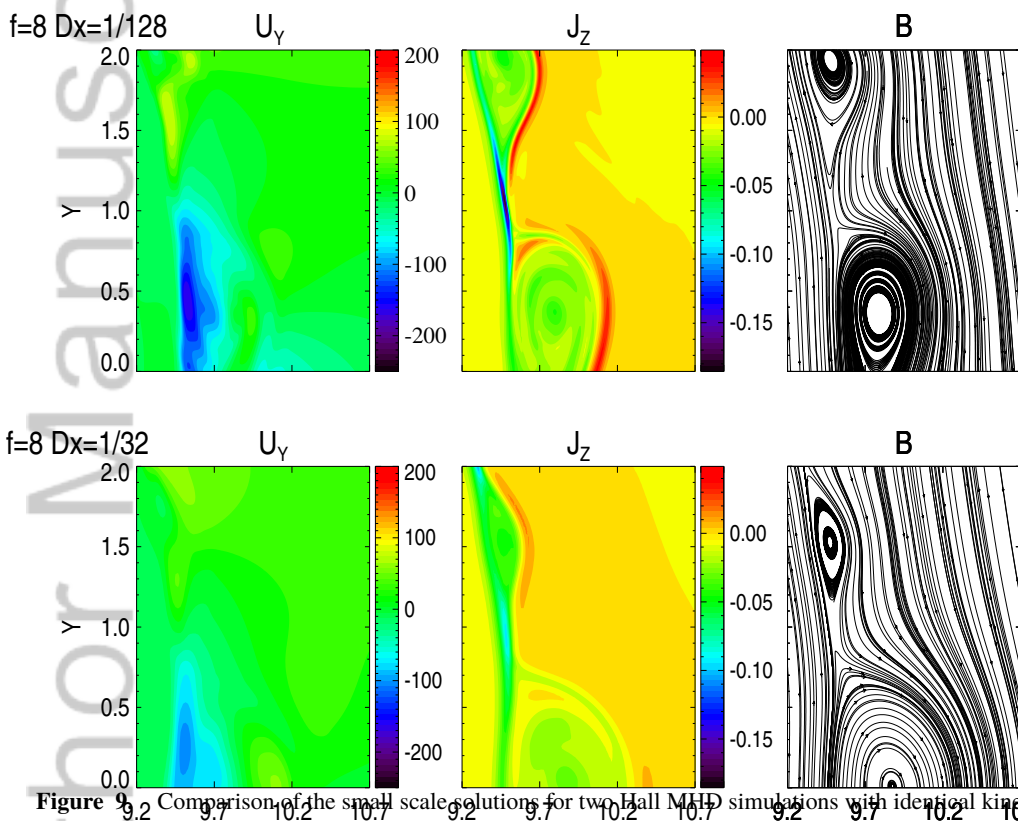
860 Vasyliunas, V. (1975), Theoretical models of magnetic field line merging, *1*, *Rev. Geophys.*
861 *Space Phys.*, *13*, 303.



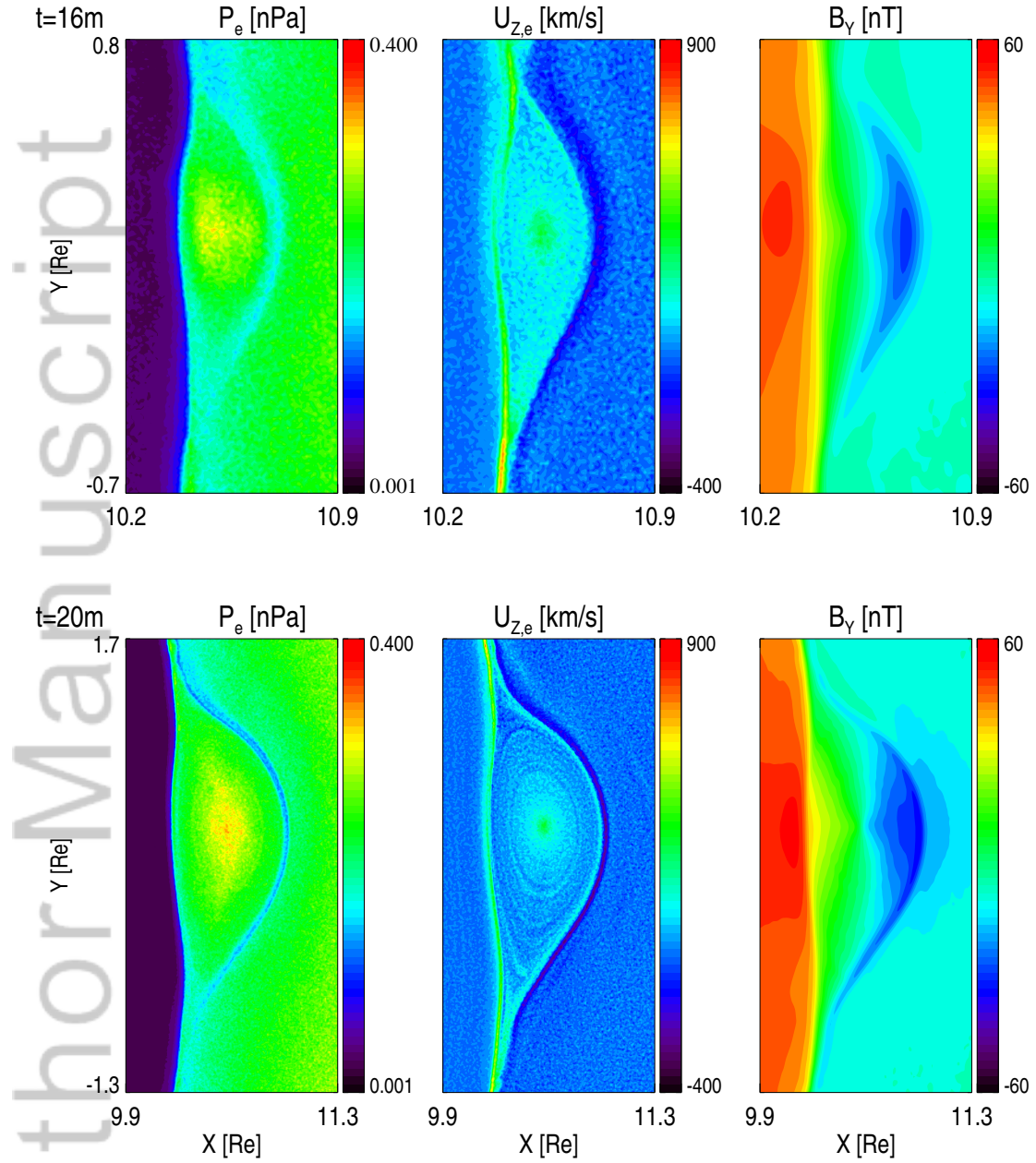
546 **Figure 7.** Time series of flux transfer events for two runs: the left column is for kinetic scaling factor $f = 8$
 547 and grid resolution $\Delta x = 1/128 R_E$, while the right column is with $f = 32$ and $\Delta x = 1/32 R_E$. The simula-
 548 tion times are shown in minutes above each plot with a 3 minute cadence. The colors show the Y component
 549 of the velocity in km/s units. The white lines are magnetic field line traces.



570 **Figure 8.** The Y and Z components of the electron velocity and the Z component of the ion velocity in km/s
 571 from the iPIC3D output. Three simulations with different f factors and grid resolutions are compared. Note
 572 that the spatial scale of the panels in the top row with $f = 8$ is four times smaller ($3/4 \times 3/4 R_E$) than in the
 573 middle and bottom rows with $f = 32$, where the panels are $3 \times 3 R_E$.

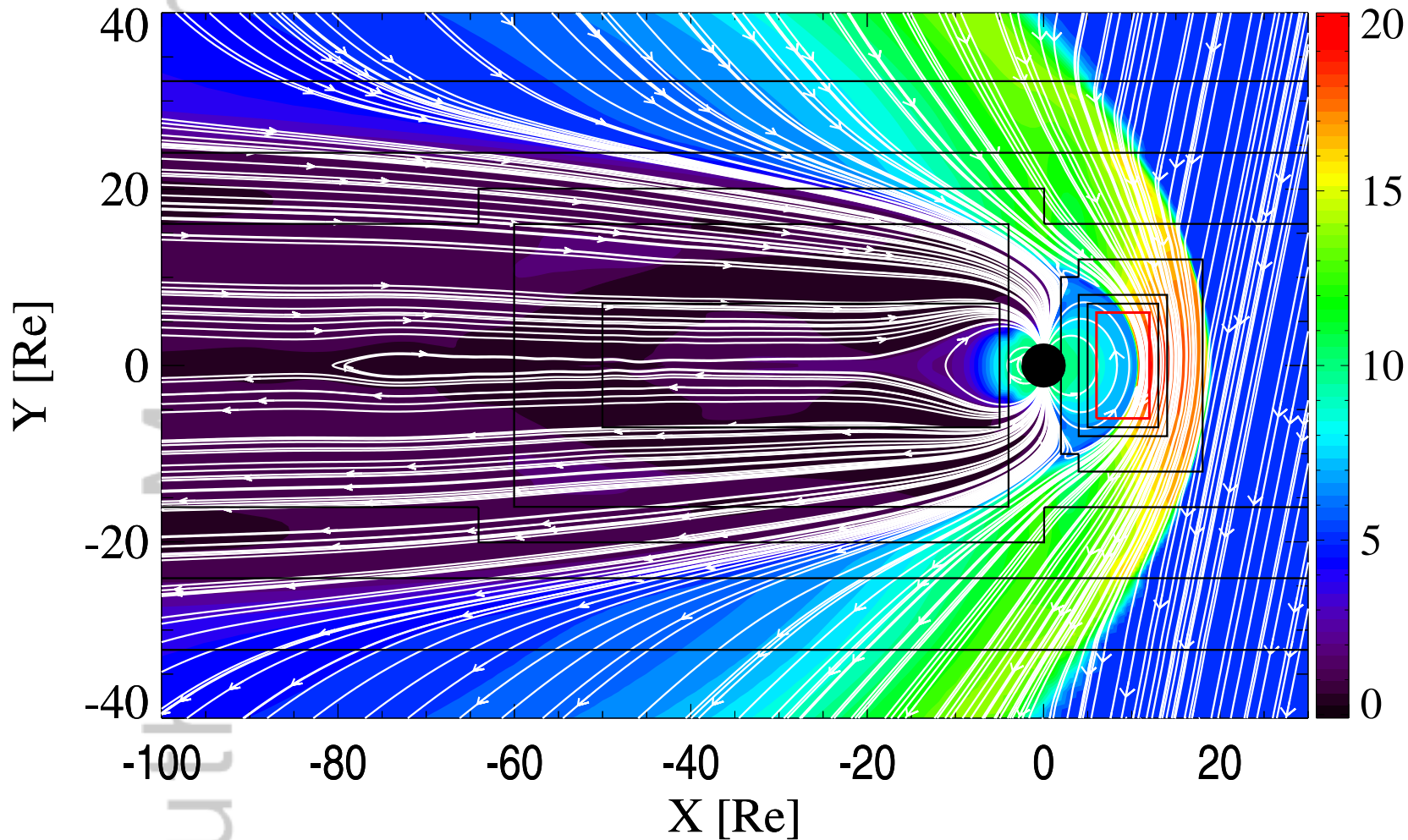


600 **Figure 9.2** Comparison of the small scale solutions for two Hall MHD simulations with identical kinetic
 601 scaling factors $f = 8$ but different grid resolutions $\Delta x = 1/128 R_E$ (top) and $1/32 R_E$ (bottom), respectively.
 602 The Y component of the ion velocity in km/s, the Z component of the current in μA and magnetic field line
 603 traces are shown for the same simulation time and same location with similar reconnection events.

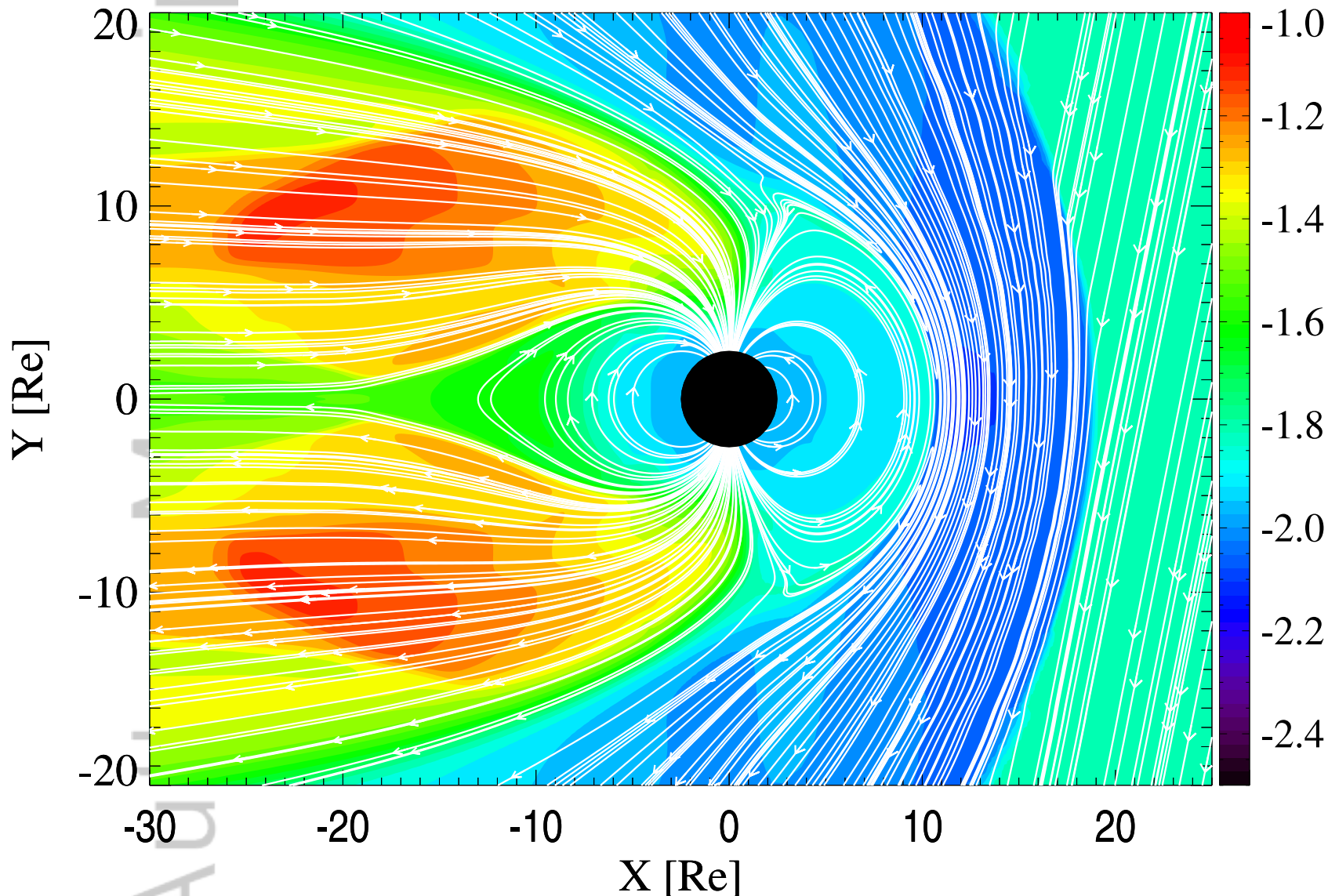


616 **Figure 10.** Evolution of an FTE in an MHD-EPIC simulation with scaling factor $f = 8$ and grid resolution
617 $\Delta x = 1/128 R_E$. The electron pressure, the out-of-plane component of the electron velocity and the Y compo-
618 nent of the magnetic field are shown for time 16 min (top) and 20 min (bottom). The spatial scales are factor
619 of 2 larger for the later time: the sizes of the panels are $0.7 \times 1.5 R_E$ and $1.5 \times 3 R_E$ in the top and bottom
620 rows, respectively.

Author Manuscript

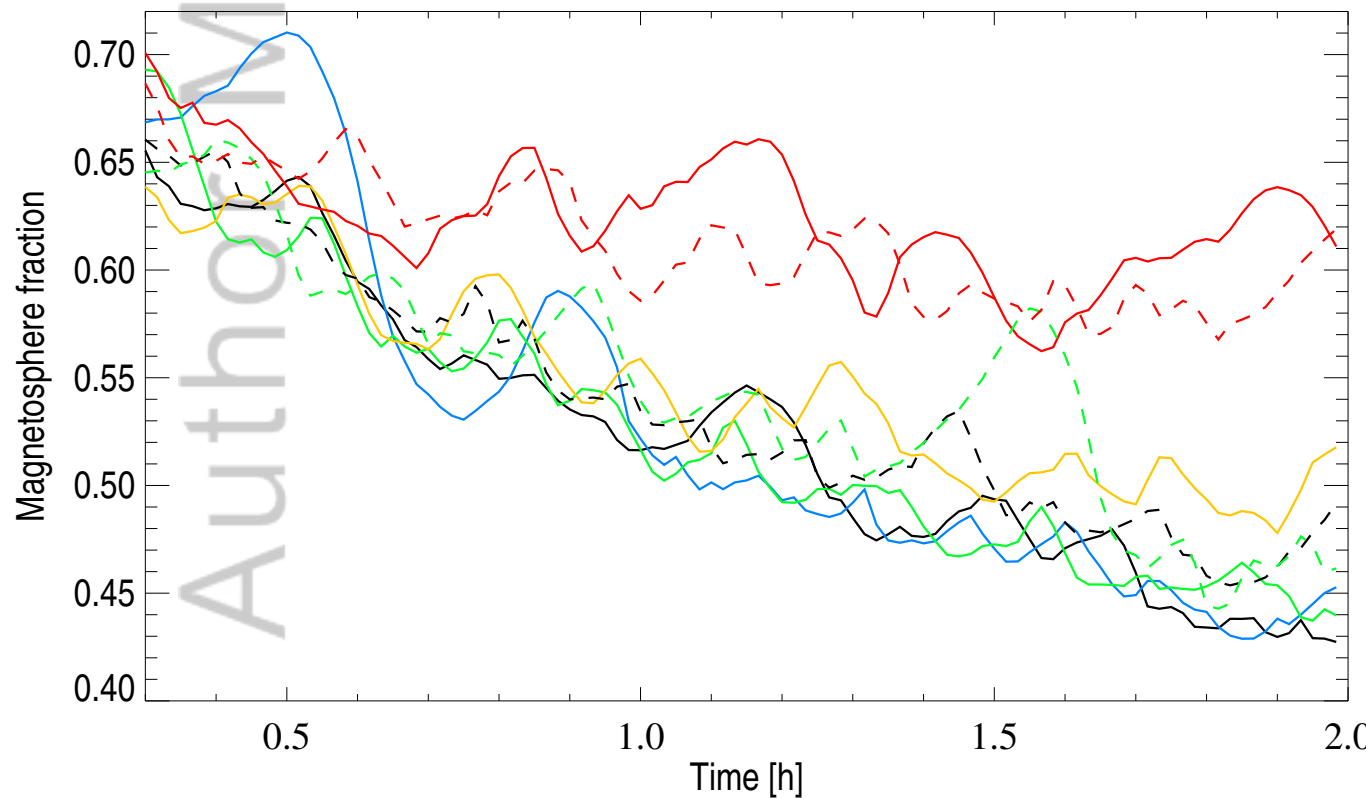
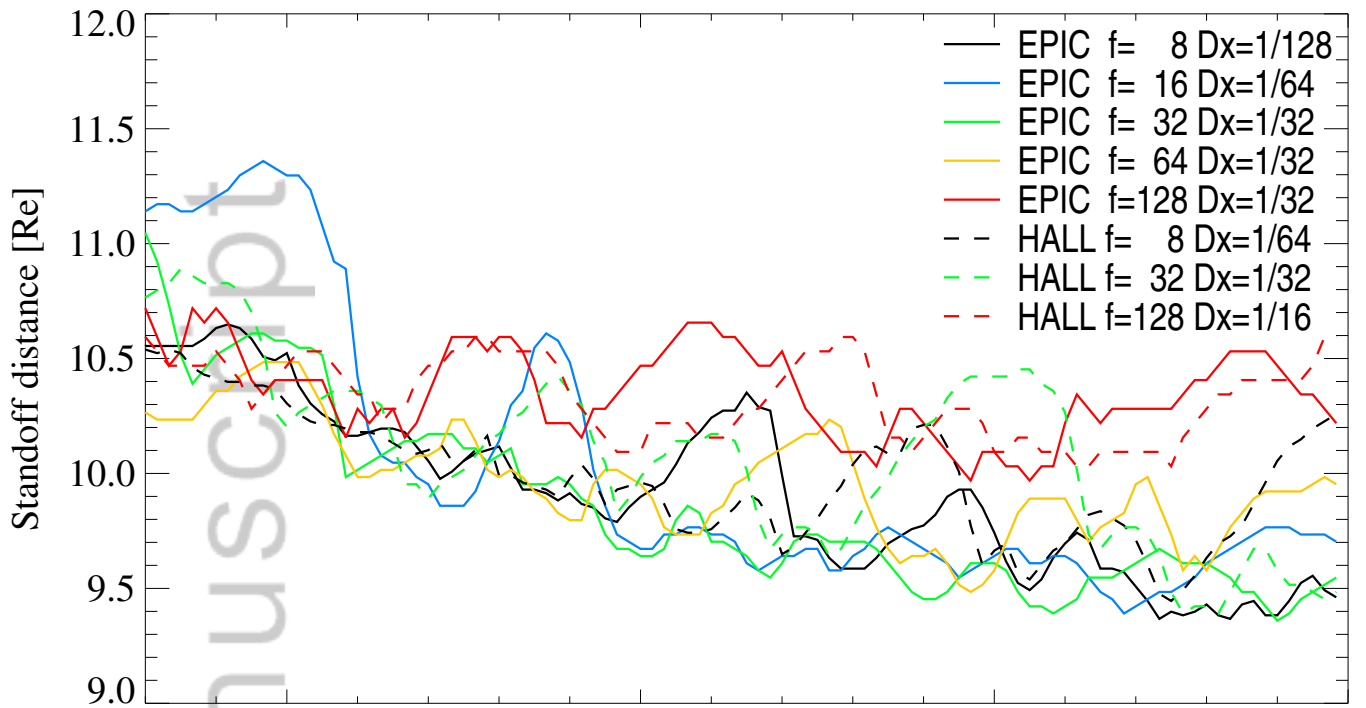


Author Manuscript



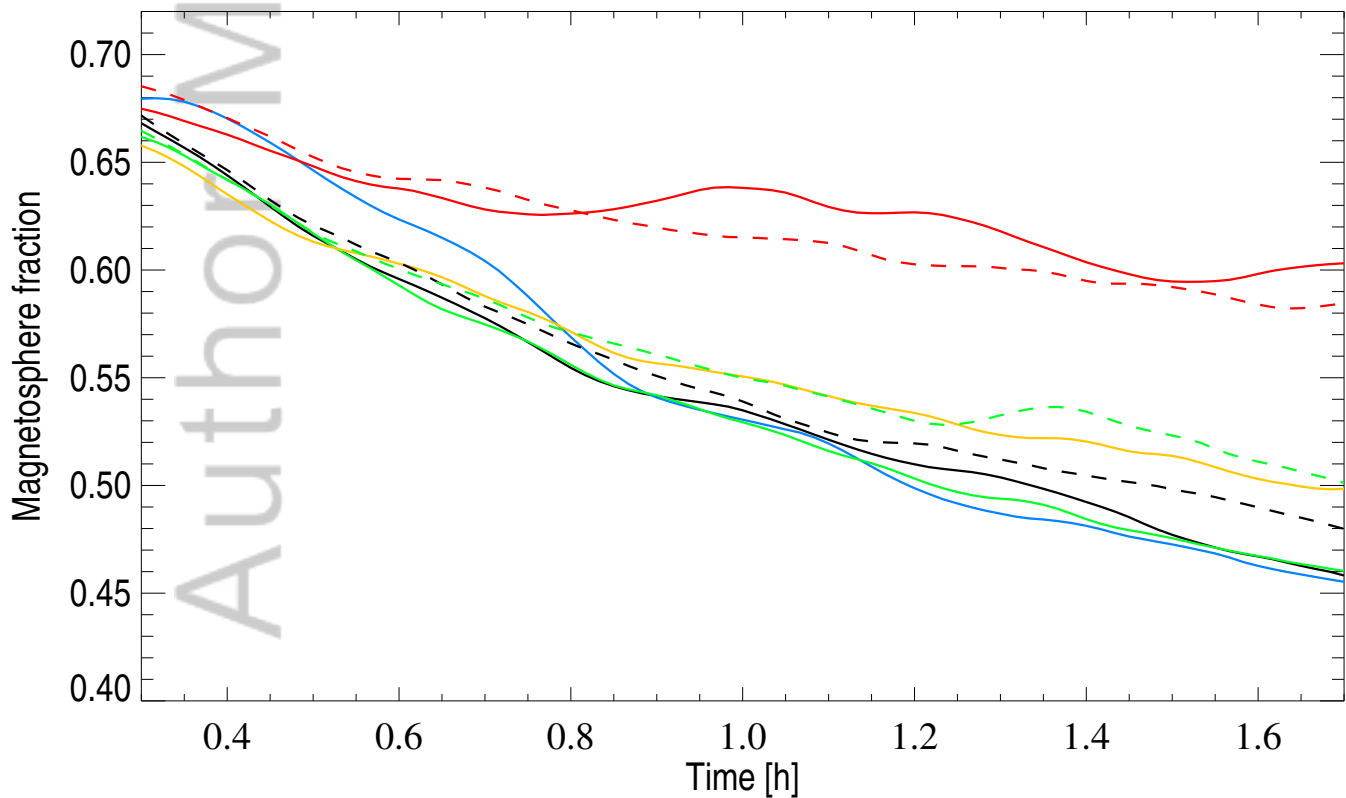
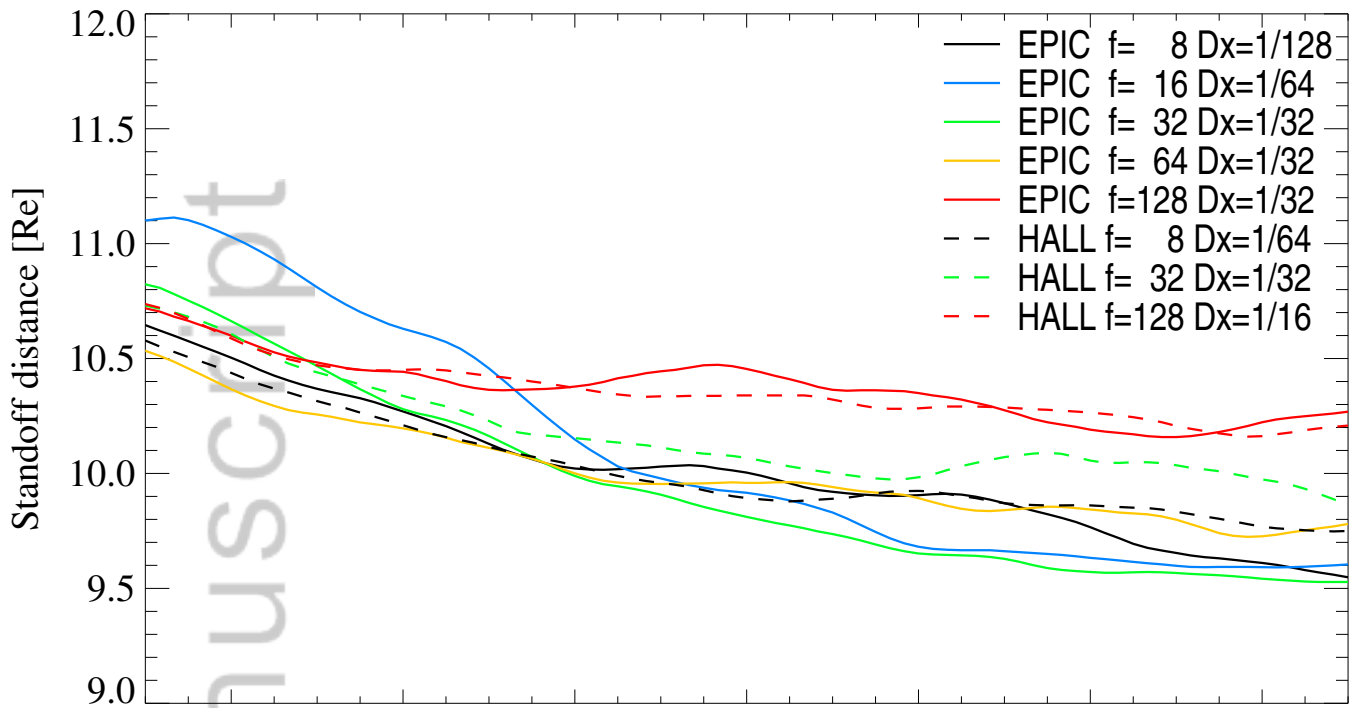
Author Manuscript

WITH GUIDE FIELD



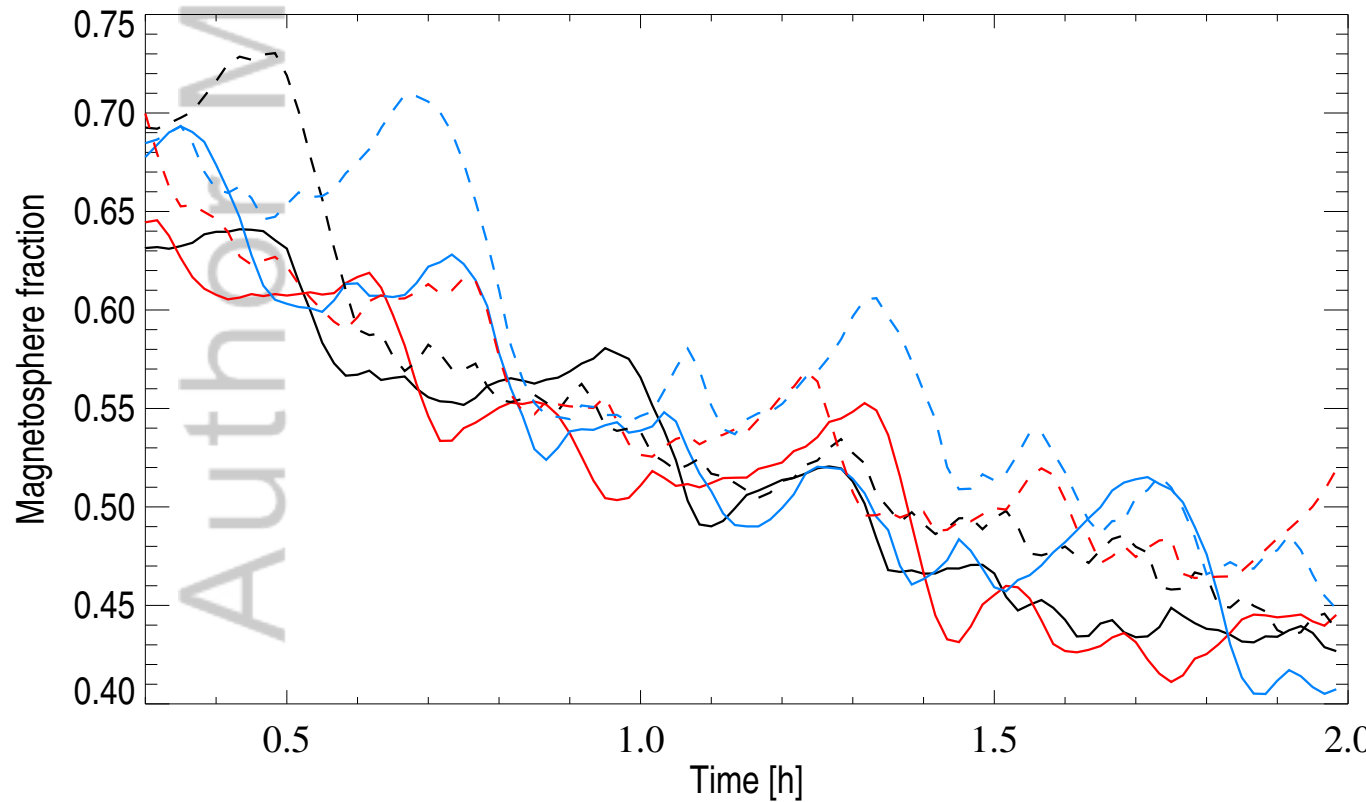
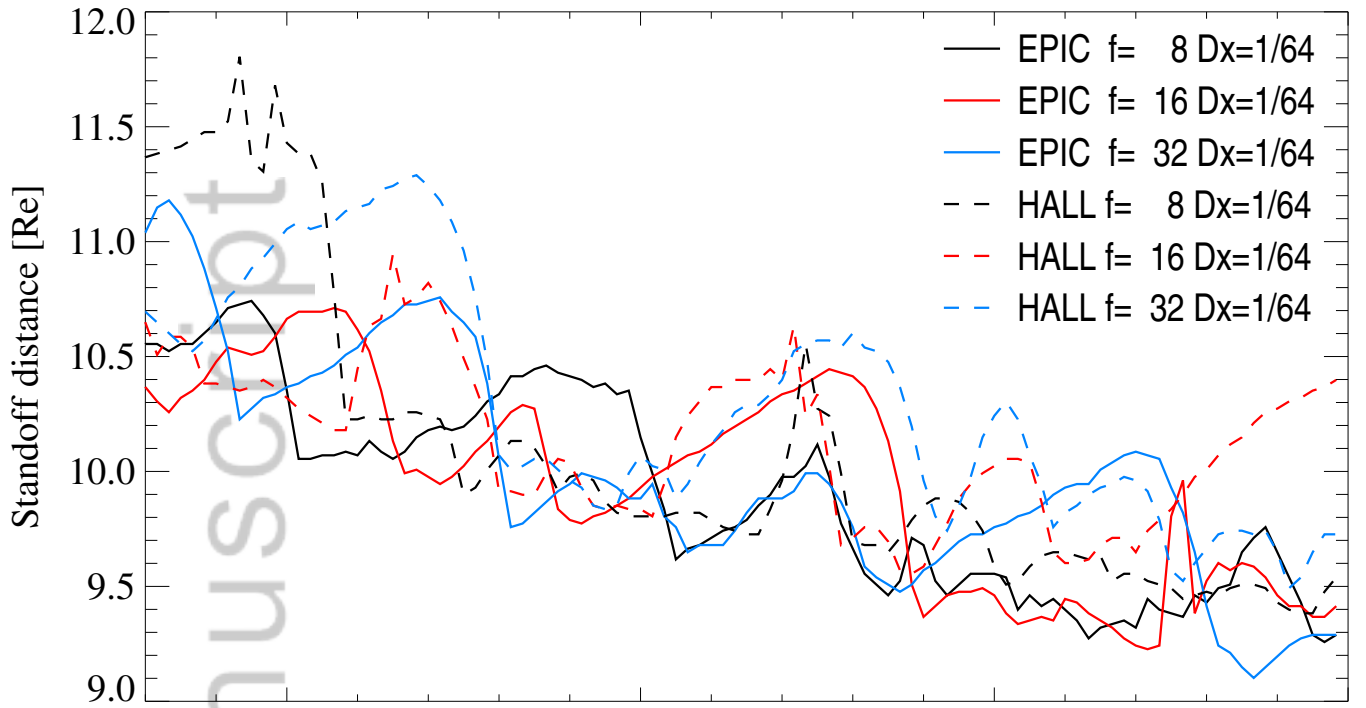
Author Manuscript

WITH GUIDE FIELD



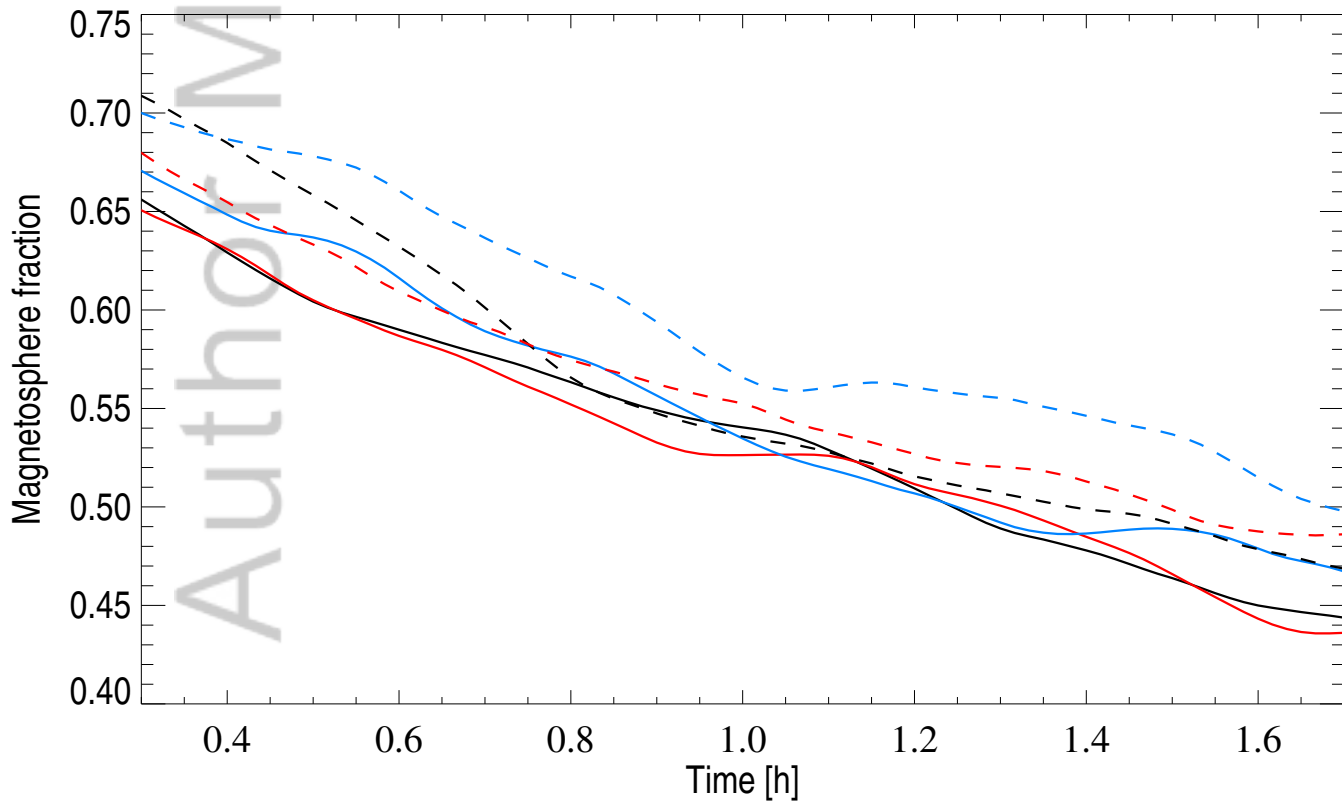
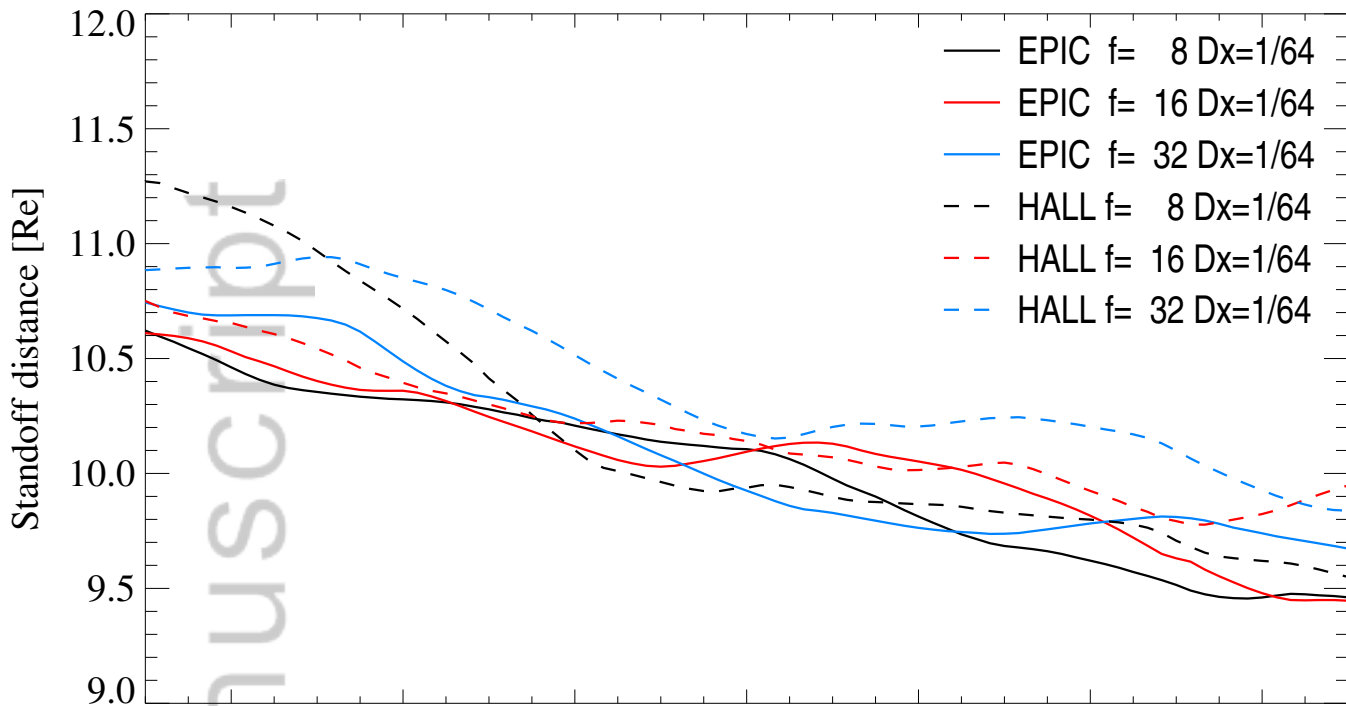
Author Manuscript

NO GUIDE FIELD

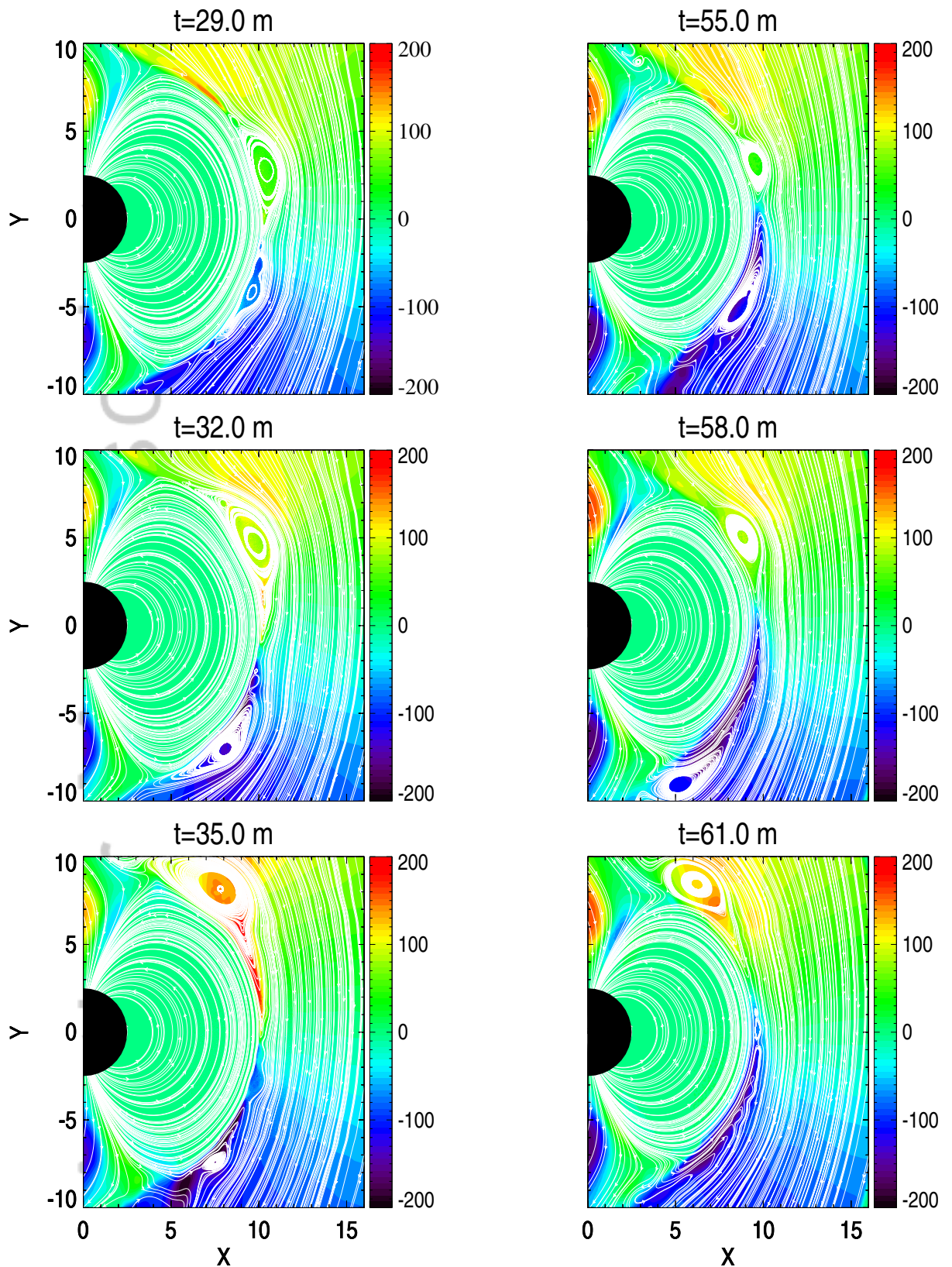


Author Manuscript

NO GUIDE FIELD

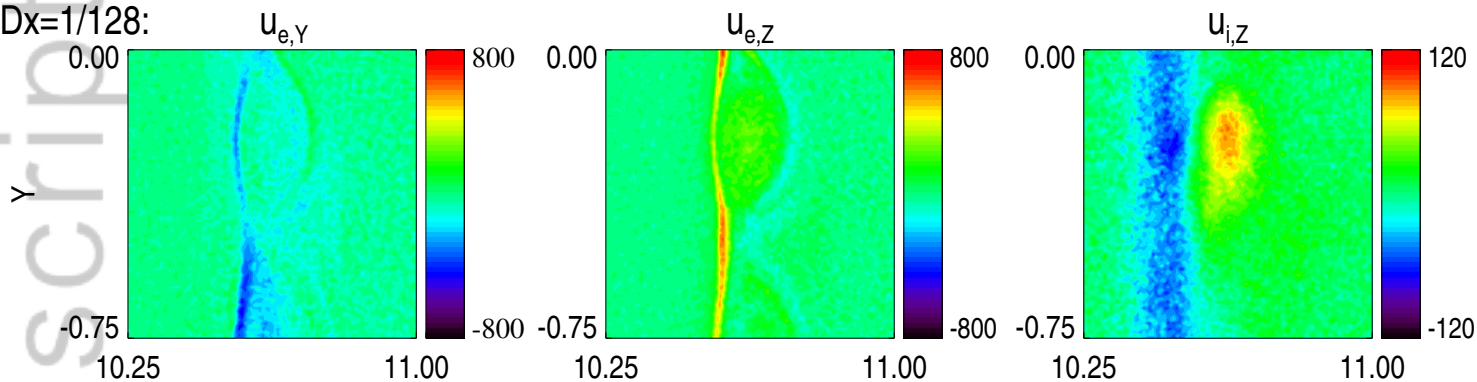


Author Manuscript

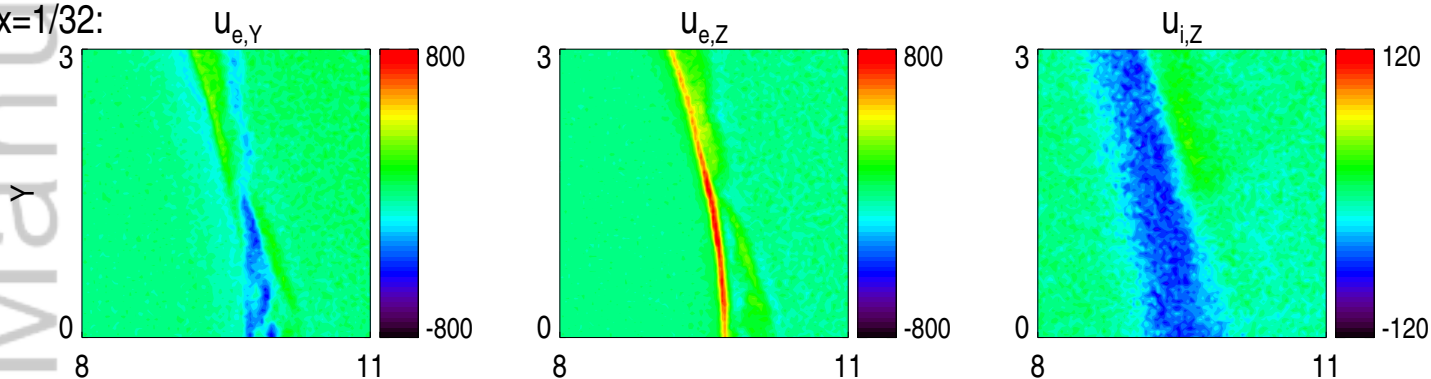


Author Manuscript

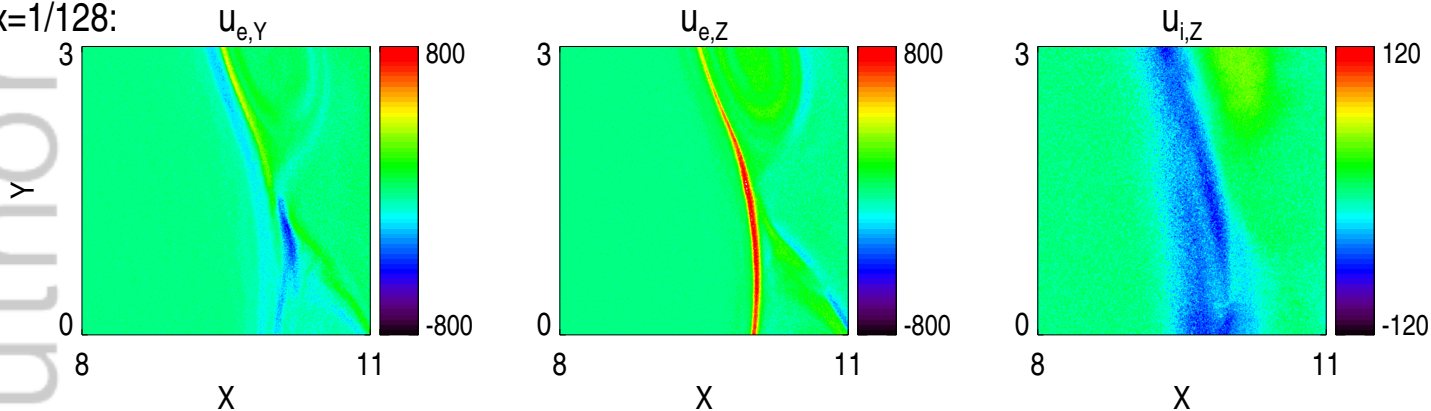
f=8 Dx=1/128:



f=32 Dx=1/32:



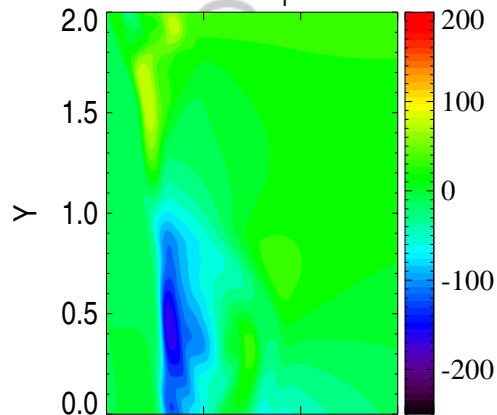
f=32 Dx=1/128:



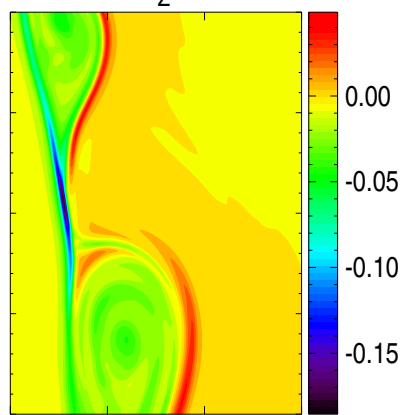
Author Manuscript

f=8 Dx=1/128

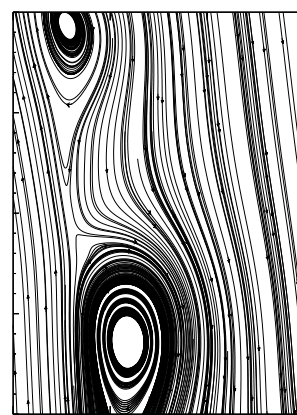
U_Y



J_Z

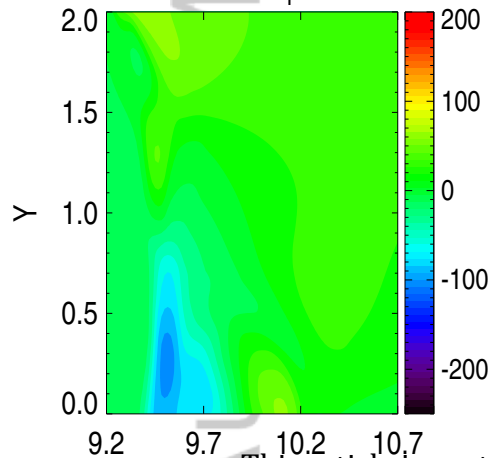


B

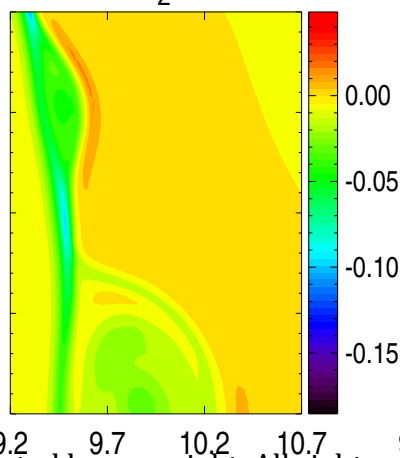


f=8 Dx=1/32

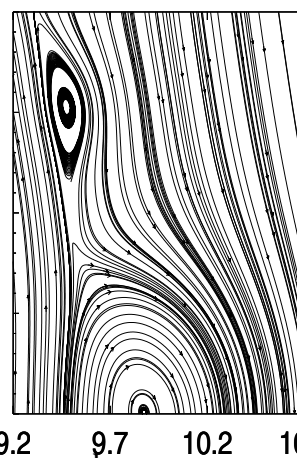
U_Y



J_Z



B



X

Author Manuscript

